VIV modelled using simplified cable dynamics coupled to sub-critical cylinder flow simulations in a moving reference frame

Lei Zhang, John Redford, Fikri Hafid, Jean-Michel Ghidaglia, Maxime Gueguin

VIV modelled using simplified cable dynamics coupled to sub-critical cylinder flow simulations in a moving reference frame

Lei Zhang[a,*], John Redford[b], Fikri Hafid[c], Jean-Michel Ghidaglia[a], Maxime Gueguin[b]

[a] *CMLA, ENS Paris-Saclay, CNRS, Université Paris-Saclay, 94235 Cachan, France*
[b] *Eurobios, 61 avenue du président Wilson, 94235 Cachan, France*
[c] *RTE-R&D, Immeuble Window, 7C place du dôme, 92073 Paris La Défense, France*

Abstract

This work focuses on the study of the phenomenon of vortex-induced vibrations in overhead lines under the effect of weak winds. Full three-dimensional simulation is not feasible because of the high length to width aspect ratios of the overhead lines. Thus a quasi-3D method based on strip theory is adopted in this work. This method decouples the system of interactions between the overhead line and the wind into a series of sub-systems. The fluid flow in each sub-system is represented as a series of independent rigid oscillating cylinder flows that are only coupled through the transmission line model. To avoid the use of a moving mesh for the fluid domain, a moving reference frame approach is employed. In this approach, the coordinate axes of the flow simulation are attached to the oscillating cylinder and an acceleration term in the flow equations accounts for the cable motion. Moreover, in order to take into account the turbulent effect in the flow, turbulence models, including RANS, LES and DES, are evaluated for the present application involving flows in the sub-critical regime. Finally, numerical test cases are performed in order to validate the turbulence models and the moving reference frame approach, then cable dynamics test cases are conducted to validate the quasi-3D method.

Keywords: fluid-structure interaction, vortex-induced vibration, strip-theory, moving reference frame, turbulence models, sub-critical circular cylinder flow

1. Introduction

This work is devoted to the study of the phenomenon of vortex-induced vibrations of long flexible circular cylinders, a phenomenon that affects overhead electrical transmission lines. Low wind speeds (approximately 1 to 10 m/s) induce vortex shedding downstream of the overhead line, creating an alternating lift force. The suspended cable is free to move laterally and vertically meaning that vibrations are induced by the alternating lift force, generating cyclic stresses that can lead to fatigue failure of the individual wire strands. Thus predicting the vibration amplitudes is essential for a better estimation of the lifespan of overhead lines.

At present, the Energy Balance Principle (EBP) is the approach used in industrial applications to assess the maximum amplitude that can occur on a conductor span during aeolian vibrations [1, 2]. This approach is based on comparison of the energy brought by the wind to the conductor and the energy dissipated through its self-damping and associated dampers at a given mode. The main limitations of this principle are that it does not take into

*Corresponding author
Email address: lzhang@cmla.ens-cachan.fr (Lei Zhang)

account the spatial and temporal variations of the wind, in addition it does not account for contributions from other spatial vibration modes.

Thus in this work, in order to have a better representation of the physics between the wind and the overhead conductor, which involves a fluid-structure interaction problem, CFD simulation is used. Generally, the numerical methods for the resolution of a fluid-structure interaction problem can be classified into two categories according to the coupling level between fluid and structure. In a monolithic method [3], a large system involving fluid and solid dynamics is solved by taking interface conditions into consideration. This type of method is robust but requires large computing resources when applied to realistic engineering problems. Whereas the second approach is a partitioned method [4], where the fluid and solid dynamics are solved separately in two different codes. Then the interface conditions are communicated from one code to the other: the fluid force is transferred from the fluid solver to the solid solver and the solid displacement is transferred inversely. This kind of method is more efficient than a monolithic method, hence it is widely used in many applications [5, 6, 7]. Moreover, it allows the use of existing codes and can take advantage of optimized formulations for each problem: fluid and solid dynamics. For example, in [6], the OpenFOAM fluid dynamics toolbox (www.openfoam.com) is coupled with the industrial structural dynamics code Code_Aster (www.code-aster.org), and in [7], the fluid dynamics code Code_Saturne (www.code-saturne.org) is coupled with Code_Aster. Due to efficiency concerns, in the present work, a partitioned method is employed with Code_Saturne to solve fluid dynamics.

Between the EBP and CFD approaches, simplified models, such as wake oscillator models [8, 9], are often used in the literature to predict VIV of cables in tension. In these models, the fluid forces due to vortex shedding in the cable wake are modelled using a dynamical system, with empirical parameters calibrated through experimental data or CFD. These models have been successfully used in marine applications, e.g. VIV modelling of risers [10, 11]. In marine applications, the ratio of the mass of fluid displaced by the cable relative to the cable mass is low, which means that the fluid structure interaction is strong. However, for overhead conductors subjected to air flow, the mass ratio is normally of the order of 2000. Much work also exists on fluid structure interactions where the vortex shedding and structural frequencies have similar orders of magnitude. This is not the case in overhead conductor applications, with vortex shedding at approximately 40 Hz and the cable fundamental frequency normally less than 1 Hz. Hence, first mode resonance cannot occur and thus excitation of the cable must come about through the harmonics of the structure's natural frequency.

However, due to the high length to width aspect ratios (of the order of several thousands) of transmission lines, three-dimensional (3-D) flow simulations at realistic Reynolds numbers are considered unfeasible. Similar to simulation of marine riser pipes [12, 13], approximate techniques known as quasi-3D methods need to be used to solve for the fluid flow. The main idea is to perform two-dimensional (2-D) simulation of air flow in 2-D sections along a transmission line, which are then linked together to account for three-dimensional flow effects, and finally the CFD simulations are coupled to the dynamics of the line. In [14, 15], the technique of strip theory is used to simulate riser response. The CFD computations are carried out in 2-D sections along a marine riser pipe, while the riser response computation is conducted in three-dimensions using a non-linear finite element code in [14] and is conducted in [15] using Euler-Bernoulli beam theory. The motion of the riser at each section affects the flow locally, such that the flow and the forces are determined individually for each section, then coupled through the motions

of the riser. In [16, 12, 17], flows around several spanwise 2-D sections of a riser are simulated, and are then linked hydrodynamically using a 3-D vortex lattice representation of the flow in the wake of the riser [12, 18]. In [19], the flow and cable variables are assumed to be periodic in the spanwise direction. The 3-D problem is transformed to a series of 2-D problems using a Fourier expansion, with each 2-D problem associated with a vibration mode. These 2-D problems are then coupled by nonlinear terms modeling the cable motion. Instead of using Code_Aster as in [7] for the structural dynamics, simplified cable models [20, 19] are preferred due to their efficiency, as shown in [21], the numerical results using the model in [20] agree well with those obtained using Code_Aster, however the simulation with the simplified model is 30-45 times faster.

Many works have focused on numerical study of vortex-induced vibration of rigid circular cylinders in two-dimensions [22, 23] or in three-dimensions with a low aspect ratio [24, 25], as has been explained previously, full-scale simulation of the 3-D problem with a high aspect ratio is not feasible. The simulation of flow around a rigid circular cylinder in two-dimensions or in three-dimensions with a low aspect ratio is an important building block for the overall cable simulation using the above-mentioned quasi-3D methods. Moreover, fluid dynamics computations for these problems enable adequate mesh resolution for the fluid domain and an appropriate turbulence model that can predict correctly the physics of the fluid flow.

The fluid flow around a rigid cylinder is influenced by a number of physical parameters, including Reynolds number, inlet free-stream turbulence level, wall roughness, etc. According to the Reynolds number, four different flow regimes can be identified with different boundary layer characteristics [26, 22]: laminar or turbulent boundary layer, separation point location, wake size, etc. For the present application with weak winds and cable diameters of approximately 30 mm, the Reynolds number is between 2×10^3 and 2×10^4. Hence the flow is in the sub-critical regime [22], meaning that the boundary layer flow remains laminar before the separation point, and the transition from laminar to turbulent flow takes place in the wake of the cylinder. Different methods are used in the literature in order to resolve circular cylinder turbulent flow, including direct numerical simulation (DNS) [25, 27], large eddy simulation (LES) [24, 28, 29], and Reynolds-averaged Navier-Stokes (RANS) simulation [22, 23, 30, 31]. DNS is not considered here because of its large computational demands. Among the RANS models, the $k-\omega$ SST model is an appropriate candidate [32, 30] for the present application that involves an adverse pressure gradient and flow separation. This model retains the near wall treatment ability of the Wilcox $k-\omega$ model and improves its behavior with respect to inlet free-stream turbulence properties [33]. In addition to the basic $k-\omega$ SST model, modifications have been introduced by several authors in order to improve its behavior under different physical conditions. In [34] the turbulent kinetic energy production term is modified in order to avoid excessive turbulent energy production in the stagnation regions. In [35] a curvature correction model is proposed to capture effects of streamline curvature and system rotation in a flow, and thus improves the accuracy of numerical results. The $k-\omega$ SST model assumes fully turbulent flow, thus adaptation of the model is required for laminar-turbulent transition modelling. In [36], the transition effect is taken into account by modifying the turbulent viscosity and empirical parameters in the basic $k-\omega$ SST model. This transition correction model is also used in [37, 38]. In LES large-scale turbulence that depends largely on the flow configuration is resolved, whereas less problem-dependant small-scale turbulence is modelled [24]. The main difficulty with LES for practical applications lies in its requirement of high grid resolution in the near-wall region [29]. In [29] LES is combined with a wall-layer model to eliminate this difficulty. Alternatively,

a hybrid RANS/LES approach can be used, which leads to Detached-Eddy Simulation (DES) [39, 40, 41]. The DES approach combines the RANS equations for the boundary layers and LES for separated flows, which results in improved separation prediction ability [40]. In this study, these three methods (RANS, LES and DES) are all used to simulate flow over a rigid circular cylinder.

Solving fluid-structure interaction problems generally involves moving computational domains and dynamic re-meshing. A general method that deals with a moving mesh is the Arbitrary Lagrangian Eulerian (ALE) formulation [42]. Alternatively, we can eliminate the difficulty of a moving mesh by attaching the coordinate axes to the cable, i.e. using a moving reference frame [43, 19]. The advantages of the moving reference frame method are multifold. Using a moving reference frame is more efficient than the ALE method, as resolution of the mesh dynamics is avoided; moreover the added steps involved in moving the ALE mesh could cause the results to be disturbed, whereas the fixed mesh does not entail such an effect. Especially as we can see later for turbulence models, the mesh size around the cylinder is essential to ensure the validity of these models.

The program adopted in this work is as follows: we begin by simulating flow around fixed and rigid circular cylinders (in two-dimensions or three-dimensions with a low aspect ratio) in order to validate turbulence models, determine appropriate grids (the problem is strongly mesh-dependent [25]), and also validate the moving reference frame approach for a fluid-structure interaction problem; afterwards, we implement a quasi-3D method based on strip theory, which is capable of simulating 3-D flows efficiently; finally we couple the quasi-3D method with a simplified cable model so as to investigate vortex-induced vibration of overhead lines. In this preliminary work, only a simple quasi-3D method is used, where the fluid flows in each 2-D section are considered independent, and the 3-D effects are only represented by the cable motion coupling. The main contributions include: evaluation and validation of different turbulence models for cylinder flows in the sub-critical regime as well as correction models to address the shortcomings of the basic $k-\omega$ SST RANS model; validation of the moving reference frame approach in combination with turbulence models, which avoids the use of a moving mesh to deal with fluid-solid interaction; validation of the quasi-3D method and its implementation through cable dynamics test cases. The goal of the present work is to present and validate a tool that can be used to evaluate wind effects on overhead conductors. In future work, this tool will be improved (e.g. a more elaborate quasi-3D method) and used to evaluate the dynamics of a realistic overhead conductor.

This paper is organized as follows. Section 2 presents the quasi-3D method, the pressure-based numerical method to solve fluid dynamics and also the moving reference frame approach to deal with fluid-structure interaction problems. Section 3 describes the turbulence models used in this work. Section 4 shows numerical results to validate the numerical methods and the turbulence models.

2. Numerical method

In this section, the quasi-3D method used in this work is first presented. This enables coupling of the fluid dynamics simulation with the cable model. The quasi-3D method divides the coupling system into a series of independent sub-systems involving fluid flow over an oscillating cylinder, which are coupled only through the cable model. A pressure-based numerical method is used for the fluid dynamics. Finally, a moving reference frame approach for a rigid body is described. This is to avoid the use of a moving mesh to capture the cable motion in

the fluid flow simulation. As with [17, 13], in the present quasi-3D method the flow around each cable section is considered as 2-D, and the 3-D effect is only taken into account through the coupling of each section in the cable model. This is justified to a certain extent in the case of lock-in, because in this situation the vortex shedding is correlated along substantial lengths of the cable. Other approaches exist to resolve the three-dimensionality of the flow around the cable. Thick strips are modelled in [44], where each cable section has a local spanwise width and the flow around each section is resolved using 3-D DNS, hence addressing the shortcomings of the quasi-3D method. In [12, 16], the flow around each cable section is solved using a 2-D Lagrangian vortex code, then a lower resolution vortex lattice model is resolved based on the 2-D results to represent the 3-D vorticity field. Finally, a source term corresponding to the 3-D vorticity field is added in the 2-D vortex code in order to account for the 3-D effect.

2.1. Quasi-3D method

For a vibrating beam of linear density m_L (i.e. the mass per unit length) that is subjected to tension H [44]

$$m_L \frac{\partial^2 \mathbf{y}}{\partial t^2} + C \frac{\partial^4 \mathbf{y}}{\partial z^4} - H \frac{\partial^2 \mathbf{y}}{\partial z^2} = \mathbf{F}(z,\, t), \tag{1}$$

where z is the coordinate in the spanwise direction of the cable, $\mathbf{y}(z,\, t)$ is the displacement of cable, $\mathbf{F}(z,\, t)$ is the fluid force per unit length, and we recover the equation (wave equation) of a vibrating string by imposing bending stiffness $C = 0$. The cable model used in this work is for straight cables, where the effect of sagging is not considered. As shown in [45], sagging can significantly influence the dynamics of an electrical cable by changing its natural frequencies and mode shapes. However, the focus here is to validate the numerical methodology with respect to the literature by simulating VIV with a simplified model. More elaborate models can be found in [20] and related the references listed in [19].

In this work, a simple quasi-3D method using strip theory [14, 44, 15] is adopted to resolve the interaction between a moving cable and its surrounding fluid flow. The cable is cut into a series of sections, and the flow over each section is simulated separately. As shown in Figure 1, the cable is discretized in space by placing N equally distributed nodes with spatial discretization length scale $\Delta z = L_z/(N-1)$, where L_z is the total length of the cable. Each node is associated with a rigid cylinder, of spanwise length L_s, since the local cable deformation caused by the fluid flow is considered to be negligible. There are no gaps between each cylinder if we take $L_s = \Delta z$. Nodes z_1 and z_N correspond to the two extremities of the cable. The bending stiffness term can be neglected for cables ($|C\frac{\partial^4 \mathbf{y}}{\partial z^4}| \ll |H\frac{\partial^2 \mathbf{y}}{\partial z^2}|$), and then equation (1) is discretized in space using a centered scheme

$$m_L \frac{\partial^2 \mathbf{y}(z_j,\, t)}{\partial t^2} - H \frac{\mathbf{y}(z_{j+1},\, t) - 2\mathbf{y}(z_j,\, t) + \mathbf{y}(z_{j-1},\, t)}{(\Delta z)^2} = \mathbf{F}(z_j,\, t). \tag{2}$$

Multiplying both sides of equation (2) by L_s and considering the contribution of neighbouring elements appearing in the space discretization as an external force, yields a mass-spring equation for each cylinder

$$M\ddot{\mathbf{y}}_j(t) + K\mathbf{y}_j(t) = \mathbf{f}_j^{\text{ext}}(t), \tag{3}$$

where mass $M = m_L L_s$, stiffness $K = 2HL_s/(\Delta z)^2$ and external force $\mathbf{f}_j^{\text{ext}}(t) = \mathbf{F}(z_j,\, t)L_s + \frac{K}{2}(\mathbf{y}_{j+1} + \mathbf{y}_{j-1})$.

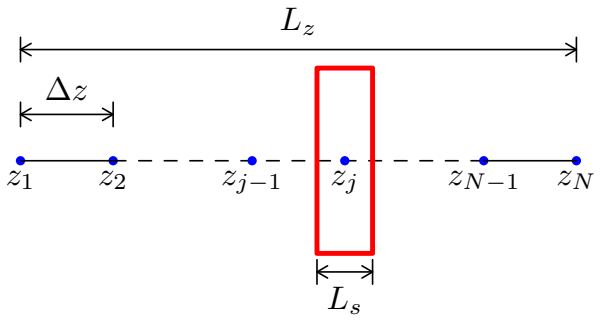

Figure 1: Illustration of the strip theory discretization.

The resulting mass-spring system is solved using the Newmark Beta method [46, pp. 121]

$$\mathbf{y}^{n+1} = \mathbf{y}^n + \Delta t\, \dot{\mathbf{y}}^n + \frac{\Delta t^2}{2}[(1-2\beta)\ddot{\mathbf{y}}^n + 2\beta\ddot{\mathbf{y}}^{n+1}], \tag{4}$$

$$\dot{\mathbf{y}}^{n+1} = \dot{\mathbf{y}}^n + \Delta t\,[(1-\gamma)\ddot{\mathbf{y}}^n + \gamma\ddot{\mathbf{y}}^{n+1}], \tag{5}$$

where Δt is the time step, and superscripts n and $n+1$ are time instants. The two parameters β, γ are taken to be $1/6$ and $1/2$ [46, pp. 122] respectively in this study.

2.2. Fluid dynamics

The industrial open-source Code_Saturne code [47] is used in this work to simulate fluid flow, and here the numerical method is briefly given in terms of time discretization. The incompressible Navier-Stokes equations are rewritten as

$$\frac{\partial \rho}{\partial t} + \nabla \cdot (\rho \mathbf{u}) = 0, \tag{6}$$

$$\rho\frac{\partial \mathbf{u}}{\partial t} - \mathbf{u}\nabla \cdot (\rho\mathbf{u}) + \nabla \cdot (\rho \mathbf{u} \otimes \mathbf{u}) = -\nabla P + \nabla \cdot \boldsymbol{\sigma} + \mathbf{s}, \tag{7}$$

where ρ is constant and we have used $\frac{\partial \rho \mathbf{u}}{\partial t} + \nabla \cdot (\rho \mathbf{u} \otimes \mathbf{u}) = \rho\frac{\partial \mathbf{u}}{\partial t} + \mathbf{u}\frac{\partial \rho}{\partial t} + \nabla \cdot (\rho \mathbf{u} \otimes \mathbf{u})$ to deduce the momentum equation, $\boldsymbol{\sigma}$ is the stress tensor and $\mathbf{s}$ is the source term. The numerical method is composed of two steps [48]:

Prediction step

Only the first-order implicit Euler scheme is considered here:

$$\rho\frac{\tilde{\mathbf{u}}^{n+1} - \mathbf{u}^n}{\Delta t} + \nabla \cdot (\tilde{\mathbf{u}}^{n+1} \otimes (\rho\mathbf{u})^n) = -\nabla P^n + \nabla \cdot \boldsymbol{\sigma}^{n+1} + \mathbf{s}^{n+1} + \tilde{\mathbf{u}}^{n+1}\nabla \cdot (\rho\mathbf{u})^n, \tag{8}$$

where the velocity is solved using explicit pressure gradient. The terms $(\cdot)^{n+1}$ can be obtained implicitly by extrapolating previous instants.

Pressure correction step

The predicted velocity does not necessarily satisfy the zero divergence condition. Thus a correction step is introduced using pressure gradient at time instant t^{n+1}:

$$\frac{(\rho\mathbf{u}^{n+1}) - (\rho\tilde{\mathbf{u}}^{n+1})}{\Delta t} = -\nabla(P^{n+1} - P^n). \tag{9}$$

Imposing the zero divergence constraint for the new time-step velocity $\nabla \cdot (\rho \mathbf{u})^{n+1} = 0$ yields the Poisson equation for the pressure at time instant t^{n+1} where only the pressure is the unknown variable. Once the new time-step pressure is obtained, the velocity can finally be found using equation (9).

2.3. Moving reference frame method

A moving reference frame attached to the rigid body is employed to avoid the use of a moving mesh for the fluid domain. The Navier-Stokes equations in a moving reference frame [43, 19] are

$$\nabla \cdot \mathbf{u} = 0, \tag{10}$$

$$\frac{\partial \mathbf{u}}{\partial t} + \mathbf{u} \cdot \nabla \mathbf{u} = -\nabla P + \nu \Delta \mathbf{u} - \frac{d\mathbf{u}^s}{dt}, \tag{11}$$

where rotation is neglected so that only translation of the rigid body is considered and $\mathbf{u}^s$ is its velocity. A detailed derivation of the Navier-Stokes equations in a moving reference frame is given in Appendix A. Neumann-type conditions remain the same as for the fixed reference frame, whereas the Dirichlet-type condition for the velocity at the inlet is rewritten as $\mathbf{u}_{\text{in}} = \mathbf{u}^*_{\text{in}} - \mathbf{u}^s$, where $\mathbf{u}^*_{\text{in}}$ is the velocity in the fixed reference frame.

Resolution of the overall system

The resolution procedure of the overall system using the quasi-3D method is illustrated in Figure 2. Each fluid solver is associated with a flow problem over an oscillating cylinder, and the cable solver resolves the overall cable dynamics. Data transfer between the fluid solvers and the cable solver is realised using MPI (Message Passing Interface) communication. The computational strategy for one iteration of the quasi-3D method is summarized as follows. In step 1, the fluid flow over an oscillating cylinder is simulated using the moving reference frame approach and the fluid force on the cylinder can thus be deduced. For step 1, a predicted cylinder motion is used in the moving reference frame approach because new time-step cylinder motion is only available after step 3. In step 2 the fluid force is transferred to the cable solver via MPI communication. Then in step 3 the mass-spring equation (3) is solved by taking into account the contribution of neighbouring cylinders on the right hand side term. The overall cable dynamics are thus obtained. Finally, in step 4 the new cable motion is communicated to the fluid solvers in order to obtain the fluid force for the next time step. These four steps can be executed iteratively for one time step to ensure that the difference between the predicted cylinder motion used in step 1 and the calculated cylinder motion obtained in step 3 is inferior to a predefined threshold, which leads to an implicit method for improved accuracy.

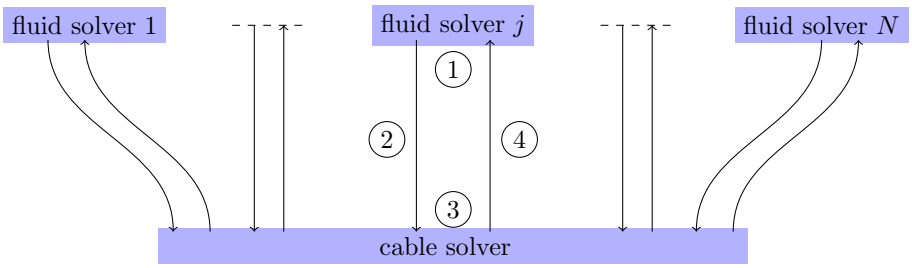

Figure 2: Resolution procedure for the quasi-3D method.

Remark. The quasi-3D method is second-order in both time and space, because the centered scheme is used in (2) for the space derivative and the Newmark Beta scheme is used for the time derivative. The CFD simulation time step length is limited by the CFL condition and the vortex shedding frequency, since a sufficient number of time steps is required during one shedding period in order to adequately capture the shedding phenomenon. On the other hand, time steps that are too small should not be used because this will lead to the checkerboard numerical problem in Code_Saturne. As for the time step when resolving the cable model, multiple time steps can be used during one time step of the CFD simulation in order to have better stability. Since the fluid force is only updated at CFD time instants, this is thus assumed to be constant during multiple cable resolution time steps. In practice, in order to improve the accuracy of the numerical results we only increase the number of sections to represent the cable, with the spatial discretization of the 2D section remaining unchanged. As can be seen below in Section 4.1, the mesh size is important to ensure the validity of the turbulence models. Nevertheless, the number of sections is limited by computing resources since each section is associated with a CFD simulation which is computationally expensive.

3. Turbulence models

The flow is turbulent at the Reynolds numbers (between 2×10^3 and 2×10^4) induced by weak winds flowing over conductor cables. In the context of this work, DNS requires excessive computing resources and so is not considered here. Appropriate models are thus required to represent turbulence effects in order to obtain reliable results within the current calculation resources. This section presents the turbulence models used in the present work, including a RANS model ($k-\omega$ SST model), a subgrid scale model for LES and a DES model based on the $k-\omega$ SST model.

3.1. $k-\omega$ SST model

The $k-\omega$ SST model [33, 32] is an appropriate candidate [30, 33] among RANS models, since we are dealing with vortex shedding phenomenon, which involves adverse pressure gradients and flow separation, as will be explained in Section 4.1. This model is a combination of the Wilcox $k-\omega$ and the standard $k-\varepsilon$ model, with the standard $k-\varepsilon$ model transformed to a $k-\omega$ model by substituting $\varepsilon = k\omega$. These two models are blended in order to take advantage of the near wall treatment associated with the Wilcox model. In addition the SST model switches to a $k-\varepsilon$ behaviour in the free-stream, thus avoiding the excessive sensitivity of the $k-\omega$ model to the inlet free-stream turbulence properties.

The equations below describe the $k-\omega$ SST model [32]

$$\frac{\partial(\rho k)}{\partial t}+\frac{\partial(\rho U_j k)}{\partial x_j}=\widetilde{P}_k-\rho\beta^* k\omega+\frac{\partial}{\partial x_j}\left[(\mu+\sigma_k\mu_T)\frac{\partial k}{\partial x_j}\right], \tag{12}$$

$$\frac{\partial(\rho\omega)}{\partial t}+\frac{\partial(\rho U_j \omega)}{\partial x_j}=\alpha\rho\frac{P_k}{\mu_t}-\rho\beta\omega^2+\frac{\partial}{\partial x_j}\left[(\mu+\sigma_\omega\mu_T)\frac{\partial\omega}{\partial x_j}\right]+2(1-F_1)\rho\sigma_{\omega2}\frac{1}{\omega}\frac{\partial k}{\partial x_i}\frac{\partial\omega}{\partial x_i}, \tag{13}$$

where $\widetilde{P}_k=\min(P_k,\,10\rho\beta^*k\omega)$, $P_k=-\rho\overline{u_i'u_j'}\frac{\partial U_i}{\partial x_j}$ represents the generation of turbulent kinetic energy, and the turbulent shear stress is given

$$-\rho\overline{u_i'u_j'}=\mu_t\left(\frac{\partial U_i}{\partial x_j}+\frac{\partial U_j}{\partial x_i}\right)-\frac{2}{3}\left(\rho k+\mu_t\frac{\partial U_i}{\partial x_i}\right)\delta_{ij}, \tag{14}$$

according to the hypothesis of Boussinesq. The generation of turbulent kinetic energy P_k can be simplified as $P_k = \mu_t S^2$ in the incompressible flow case, where $S = \sqrt{2S_{ij}S_{ij}}$, the strain rate tensor $S_{ij} = \frac{1}{2}\left(\frac{\partial U_i}{\partial x_j} + \frac{\partial U_j}{\partial x_i}\right)$. Moreover, production of turbulent kinetic energy is limited to a maximum of $10\rho\beta^* k\omega$ in order to prevent the build-up of turbulence in the stagnation region [40].

The blending function F_1 which appears in equation (13) and is used to switch between the $k-\varepsilon$ and $k-\omega$ formulations in the near wall region and far field, is given by

$$F_1 = \tanh\left\{\left\{\min\left[\max\left(\frac{\sqrt{k}}{\beta^*\omega y}, \frac{500\nu}{y^2\omega}\right), \frac{4\rho\sigma_{\omega 2}k}{CD_{k\omega}y^2}\right]\right\}^4\right\}, \tag{15}$$

where

$$CD_{k\omega} = \max\left(2\rho\sigma_{\omega 2}\frac{1}{\omega}\frac{\partial k}{\partial x_i}\frac{\partial \omega}{\partial x_i}, 10^{-10}\right). \tag{16}$$

The blending function F_1 is also used to determine the constants $(\sigma_k, \cdots)$ in the model by combining the associated constants in the original $k-\omega$ model $(\sigma_{k1}, \cdots)$ and in the transformed $k-\varepsilon$ model $(\sigma_{k2}, \cdots)$:

$$\phi = F_1\phi_1 + (1-F_1)\phi_2. \tag{17}$$

The values of the constants in the model are

$$\beta^* = 0.09,\ \sigma_{k1} = 0.85,\ \sigma_{k2} = 1,\ \sigma_{\omega 1} = 0.5,\ \sigma_{\omega 2} = 0.856,\ \alpha_1 = \frac{5}{9},\ \alpha_2 = 0.44,\ \beta_1 = \frac{3}{40},\ \beta_2 = 0.0828. \tag{18}$$

The turbulent viscosity is calculated by

$$\mu_T = \rho k \cdot \min\left(\frac{1}{\omega}, \frac{a_1}{S\cdot F_2}\right), \tag{19}$$

where $a_1 = 0.31$ and

$$F_2 = \tanh\left[\left[\max\left(\frac{2\sqrt{k}}{\beta^*\omega y}, \frac{500\nu}{y^2\omega}\right)\right]^2\right]. \tag{20}$$

In addition to the basic $k-\omega$ SST model introduced above, a curvature correction model [35] is developed in order to capture effects of streamline curvature. The curvature correction model uses a multiplier f_{r1} for the production terms (P_k and $\alpha\rho S^2$ respectively in the transport equations for k and ω) in the $k-\omega$ SST model:

$$f_{r1} = \max\{\min(f_{\text{rotation}}, f_r^{\max}), 0\}, \tag{21}$$

where $f_r^{\max}$ is a parameter that can be calibrated using numerical test cases and function f_{rotation} is defined as

$$f_{\text{rotation}} = (1+c_{r1})\frac{2r^*}{1+r^*}\left[1 - c_{r3}\tan^{-1}(c_{r2}\tilde{r})\right] - c_{r_1}, \tag{22}$$

where empirical constants c_{r1}, c_{r2} and c_{r3} are set equal to 1, 2 and 1 respectively, and the two arguments of the previous function are defined as:

$$r^* = \frac{S}{\Omega}, \tag{23}$$

$$\tilde{r} = 2\Omega_{ik}S_{jk}\frac{dS_{ij}}{dt}\frac{1}{\Omega D^3}, \tag{24}$$

where $\Omega_{ij} = \frac{1}{2}\left(\frac{\partial u_i}{\partial x_j} - \frac{\partial u_j}{\partial x_i}\right)$, $\Omega = \sqrt{2\Omega_{ij}\Omega_{ij}}$ and $D = \sqrt{\max(S^2,\, 0.09\omega^2)}$.

The $k-\omega$ SST model assumes a fully turbulent flow in the whole domain. However, for the present application with flow over a cylinder, the flow is in the sub-critical regime, i.e. the boundary layer flow around the cylinder remains laminar before the separation point and laminar-turbulent transition occurs in the wake of the cylinder. Transition models requiring supplementary transport equations may be more appropriate [49] and will be studied in future work. Here we consider only a transition correction for the $k-\omega$ SST model used in the literature [37, 38, 36] based on the viscosity ratio $R_T = \frac{\mu_t}{\mu} = \frac{\rho k}{\mu\omega}$. The transition correction consists of

- damping of the turbulent viscosity

$$\mu_t = \rho k \cdot \min\left(\frac{\alpha^*}{\omega},\, \frac{a_1}{S \cdot F_2}\right), \text{ with } \alpha_1^* = \frac{0.024 + R_T/6}{1 + R_T/6},\, \alpha_2^* = 1, \tag{25}$$

- damping of the turbulent kinetic energy sink term with β^* in $\beta^* k\omega$ recalculated by

$$\beta^* = F_1\beta_1^* + (1 - F_1)\beta_2^*, \text{ where } \beta_1^* = 0.09\frac{5/18 + (R_T/8)^4}{1 + (R_T/8)^4},\, \beta_2^* = 0.09, \tag{26}$$

- damping of the specific dissipation rate source term with α in $\alpha\rho S^2$ recalculated by

$$\alpha = F_1\alpha_1 + (1 - F_1)\alpha_2, \text{ where } \alpha_1 = \frac{5}{9}\frac{0.1 + R_T/2.7}{1 + R_T/2.7},\, \alpha_2 = 0.44. \tag{27}$$

3.2. LES: Smagorinsky model

In LES two turbulence scales are considered and a spatial filter is used to separate them [24]. Large-scale flow features are resolved directly, whereas the small-scale turbulence effects, which are less problem-dependent, are represented by simple models. Here only the Smagorinsky model [50] is considered, giving

$$\sigma_{ij}^a = -2\nu_T S_{ij}, \tag{28}$$

where σ_{ij}^a is the anisotropic part of the subgrid scale Reynolds stress. The eddy viscosity ν_T is determined using the strain rate tensor S_{ij} and the subgrid length l:

$$\nu_T = l^2 S, \tag{29}$$

where $l = C_s\Delta$ is proportional to filter width Δ and C_s is the Smagorinsky constant.

3.3. $k-\omega$ SST DES model

The DES method is a hybrid RANS/LES approach that utilises a RANS model in low grid resolution areas and the LES formulation for sufficiently fine grid resolution areas [41]. RANS is used in boundary layers to avoid the need for excessive mesh refinement, and in separated regions LES is used to improve the separation prediction capability [39, 51, 41]. The DES formulation based on the $k-\omega$ SST model is employed here by modifying the dissipation term in the k-equation:

$$\beta^*\rho k\omega \longrightarrow \beta^*\rho k\omega F_{\mathrm{DES}}, \text{ with } F_{\mathrm{DES}} = \max\left(\frac{L_t}{C_{\mathrm{DES}}\Delta},\, 1\right), \tag{30}$$

where the switch from RANS to LES is achieved by comparing the RANS turbulence length scale $L_t = \frac{\sqrt{k}}{\beta^* \omega}$ to the LES turbulence length scale $C_{\mathrm{DES}}\Delta$, where Δ is the local grid spacing, and C_{DES} is an empirical DES formulation constant. Moreover, in order to avoid the switch from RANS to DES occurring inside the boundary layer, which reduces the accuracy of the separation prediction, the DES limiter is altered to

$$F_{\mathrm{DES}} = \max\left(\frac{L_t}{C_{\mathrm{DES}}\Delta}(1 - F_2),\, 1\right), \tag{31}$$

where F_2 is given by (20).

4. Numerical results

As mentioned previously, the quasi-3D method is composed of several elements: a cable is divided into 2-D sections or in some cases, 3-D sections with a low aspect ratio are used to investigate 3-D effects; then each section is considered as a fluid-structure interaction problem and is solved independently; finally the quasi-3D method is used to couple the different sections in order to simulate the overall cable dynamics. Numerical results are presented in this section to validate the numerical method presented in Section 2 and the turbulence models in Section 3. Flow over a fixed circular cylinder is first simulated in order to validate the turbulence models. Then flow over a flexibly mounted cylinder is considered for validation of the moving reference frame method to treat fluid-structure interaction problems. Finally, the cable dynamics are simulated using the quasi-3D approach. For weak winds flowing over electrical lines, the Reynolds number based on the line sectional diameter and wind velocity is typically between 2×10^3 and 2×10^4, which corresponds to a sub-critical cylinder flow, as will be explained in detail below. Therefore, in the rigid cylinder flow test cases here $\mathrm{Re} = 10^4$. Then benchmark marine applications, where mass ratios are small, are simulated in order to validate the numerical methodology. For the laminar cases, vortex shedding frequency and cable fundamental frequency are of similar order, and for the turbulent case, the maximal vortex shedding frequency is about 20 times the cable fundamental frequency. However, in overhead conductor applications the ratios of cable material to fluid mass and vortex shedding to cable fundamental frequency are high. Simulation of realistic overhead conductor applications will be presented in future work.

4.1. Flow over a fixed circular cylinder

The flow over a fixed circular cylinder is first considered, as shown in Figure 3, where the angle θ is in the clockwise direction from the upstream stagnation point $A\,(\theta = 0)$. In Figure 4, a typical pressure coefficient distribution around a circular cylinder as a function of θ is presented, with the following definition for the pressure coefficient C_P

$$C_P = \frac{P - P_0}{\frac{1}{2}\rho U_0^2}, \tag{32}$$

where P_0 and U_0 are respectively the free stream pressure and velocity, and ρ is the fluid density. At the stagnation point A, the pressure attains its maximum. Then from point A to point B, the pressure drops as the flow is accelerated. The pressure eventually becomes lower than the reference pressure P_0 at $C_P = 0$, and then attains its minimum where the velocity at its maximum at $\theta \approx 90^\circ$. Afterwards, the adverse pressure gradient means that the velocity decreases, and eventually separation occurs.

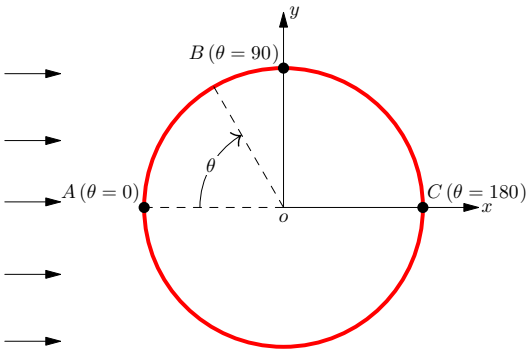

Figure 3: Cylinder coordinate system.

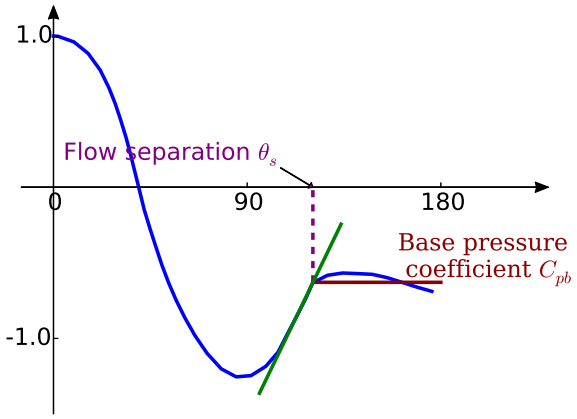

Figure 4: Pressure distribution C_P around a circular cylinder [23].

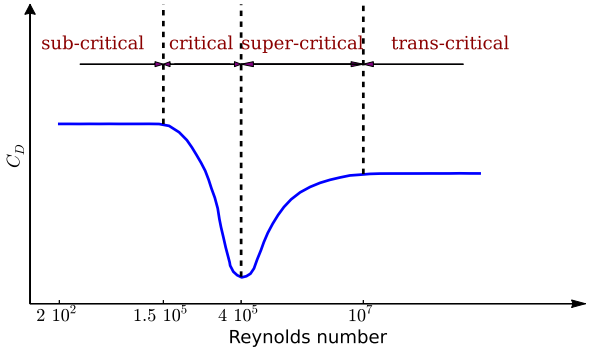

Figure 5: Illustration of the 4 flow regimes: drag coefficient as a function of the Reynolds number.

Due to the instability of flow separation, vortices shed periodically from lower and upper part of the cylinder, thus the well-known von Karman vortex street develops. For our application, particular attention is paid to the determination of fluid forces on the cylinders, including the drag and lift forces. These forces are then coupled with the cable dynamics in order to evaluate cable motion. Two non-dimensional numbers are thus defined: the mean drag coefficient C_D, the root-mean-square lift coefficient r.m.s. $C_{L,\,\mathrm{rms}}$.

$$C_D = \frac{F_D}{\frac{1}{2}\rho U_0^2 D} \text{ and } C_{L,\,\mathrm{rms}} = \frac{F_{L,\,\mathrm{rms}}}{\frac{1}{2}\rho U_0^2 D}, \tag{33}$$

where F_D and $F_{L,\,\mathrm{rms}}$ are respectively the time-averaged drag force per unit length and root-mean-square lift force per unit length, and D is the diameter of the cylinder. Another important non-dimensional number is the Strouhal number, that relates the shedding frequency to the velocity of the flow and a characteristic dimension of the body,

$$\mathrm{St} = \frac{f\,D}{U_0}, \tag{34}$$

where f is the vortex shedding frequency.

For smooth cylinders, four regimes can be distinguished according to the Reynolds number ($\mathrm{Re} = \frac{\rho U_0 D}{\mu}$) with different flow characteristics [26, 22] (e.g. separation point, base pressure coefficient C_{pb}, etc.). These regimes are

sub-critical flow $2\times10^2 < \mathrm{Re} < 1.5\times10^5$, critical flow $1.5\times10^5 < \mathrm{Re} < 4\times10^5$, super-critical flow $4\times10^5 < \mathrm{Re} < 10^7$, trans-critical flow $\mathrm{Re} > 10^7$. In Figure 5 the dependence of drag coefficient on flow regimes is illustrated. For the present application, the cable diameter is about 3 cm, the inlet wind velocity is between 1 and 10 m/s, which corresponds to Reynolds numbers between 2×10^3 and 2×10^4, thus the flow is in the sub-critical regime. In this flow regime the boundary layer remains laminar [22], and the drag coefficient $C_D \approx 1.0 - 1.2$, is not dependent on Re (Figure 5). The Strouhal number $\mathrm{St} \approx 0.2$, and the location of separation ϕ_s is between 75° and 85°. A transition from laminar to turbulent flow occurs behind the separation point and in the region where the wake is formed. The flow characteristics of the other regimes can be found in [22].

Computational domain. The computational domain is depicted in Figure 6, and the outer edge of the domain is circular as in [24, 22], with a radius extended to $20D$ in order to avoid boundary effects. The circular arc with radius $r = 20D$ and $\theta \in \{-\pi/2, \pi/2\}$ forms the inlet boundary, and the circular arc $r = 20D$ and $\theta \in \{\pi/2, 3\pi/2\}$ forms the outlet boundary.

In order to capture the vortex shedding phenomenon, the mesh needs to be refined at the wall. The dimensionless wall distance y^+ which can be used to specify the mesh resolution at the wall, has the following definition:

$$y^+ = \frac{yu^*}{\nu}, \tag{35}$$

where ν is the kinematic viscosity, and the friction velocity at the wall u^* is defined as $u^* = \sqrt{\tau_w/\rho}$, where τ_w is the wall shear stress. To correctly resolve the viscous sublayer, it is necessary to place at least a few cells within the $y^+ < 5$ region and to have the first cell adjacent to the cylinder at $y^+ \approx 1$ [30].

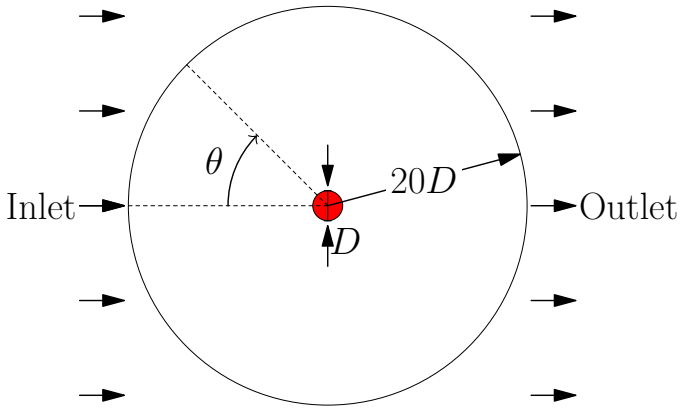

Figure 6: Computational domain where the cylinder is represented by the red disk.

Boundary conditions. For the $k-\omega$ SST model, the following boundary conditions are used for k and ω:

- At the inlet, the turbulent kinetic energy can be specified using $k = \frac{3}{2}(I|u_{\mathrm{ref}}|)^2$, where I is the turbulent intensity and u_{ref} is a reference velocity. The specific rate of dissipation ω can either be defined using the turbulence length scale $\omega = \frac{\sqrt{k}}{l}$, or the turbulent viscosity $\omega = \frac{k}{\nu_t}$. These two methods for definition of ω at the inlet can be used to double-check the resulting turbulent viscosity or turbulence length in order to make sure that reasonable values are given.

- At the wall, Menter [32] recommends the use of $k = 0$, $\omega = \dfrac{60\nu}{\beta_1(\Delta y_1)^2}$, where Δy_1 is the distance to the next point away from the wall.

4.1.1. 2-D simulation

The numerical results of two 2-D test cases at different Reynolds numbers are presented in this section to evaluate the $k-\omega$ SST model.

Case: $Re = 10^6$. A super-critical flow with $\mathrm{Re} = 10^6$ is first considered, whereas for our application of weak winds on overhead lines, the flow is in the sub-critical regime. The $k-\omega$ SST model is used with Menter's formulation for ω at the wall. At the inlet, turbulent intensity $I = 0.2\%$ and turbulent viscosity $\nu_t = \nu$ [31] are used to determine the boundary conditions for k and ω. The simulation yields $\mathrm{St} = 0.289$, $C_{L,\,\mathrm{rms}} = 0.183$, $C_D = 0.523$, which correspond well to results presented in [29, 31]. In Figure 7, the mean pressure distribution on the cylinder is compared with other simulations from the literature [29, 31]. The LES and the RANS simulation from Catalano et al. [29] are 3-D computations. So we can expect the physical representation to be more complete in these two cases. A smaller base pressure coefficient with respect to the 3-D simulation is obtained here, which is coherent with the fact that 3-D simulation tends to decrease the drag force [52].

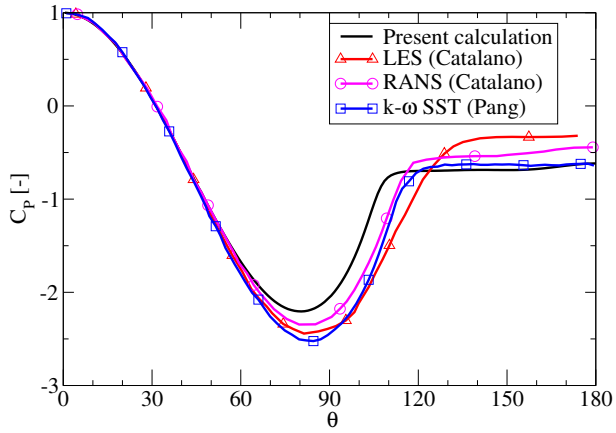

Figure 7: Mean pressure distribution on the cylinder.

The numerical result can be improved by for example considering a 3-D simulation or by using a more refined mesh in the wake. However, since our interest lies primarily in the sub-critical regime, 3-D simulation and mesh refinement are not performed for this Reynolds number. The objective here is to show that the $k-\omega$ SST model with Menter's boundary condition for ω at the wall works well at this super-critical regime. In this case the boundary layer becomes turbulent before the separation point, which is not the case in the sub-critical regime, but this has allowed validation of the turbulence model.

Case: $Re = 10^4$. As in [30], for this test case turbulent intensity $I = 0.2\%$ and turbulence length scale $l = 0.1D$ are specified at the inlet to determine the free stream turbulence level, which corresponds to a turbulence viscosity of $\nu_t = 2.5\nu$. The time step Δt is set to be $\frac{T_{\mathrm{vortex}}}{200}$, where T_{vortex} is the vortex shedding period, which can be estimated using the Strouhal number. Menter's boundary condition for ω at the wall is used and Figures 8 and 9

(blue line) show the calculated lift and drag coefficients (Run **1**). The values in Table 2 show that these forces are over-predicted by the present calculation compared with the literature values listed in Table 1. The mesh resolution at the wall is verified, for the present calculation without use of the wall function, y^+ is ensured to be around 1 as shown in Figure 10. The y^+ value is also verified for all the turbulence modelling approaches listed in Table 2 in order to confirm that its value is around 1.

The difference between the present simulation and the reference data could be explained by the two following considerations. First, at $\mathrm{Re} = 10^4$, the flow is in the sub-critical regime, meaning that the flow remains laminar before the separation point. However, the $k-\omega$ SST model assumes that the flow is turbulent throughout the domain. Thus, use of a transition model could improve the results [49] and this will be studied in future work. Only some adaptations of the $k-\omega$ SST model to the sub-critical regime are tested here. Second, the flow is considered 2-D for the present calculation, whereas for most of the reference data listed in Table 1 the 3-D flow is simulated. At such a Reynolds number, the 3-D effect is important [52], which will result in a reduction in the fluid forces due to the effect of spanwise components of the Reynolds stresses. Therefore, some 3-D calculations with the use of transition correction models are now carried out.

Before performing 3-D simulations, a 2-D test using a small value for ω at the wall [53] (Run **2**) to account for the transition effect is simulated. It is seen in Figures 8 and 9 (red line) that the resulting lift and drag coefficients of Run **2** are closer than Run **1** to that reported in the literature ($C_{L,\,\mathrm{rms}} \in [0.36-0.64]$ and $C_D \in [1.1-1.2]$). In Figure 11, the pressure distribution on the cylinder obtained by these two numerical calculations are compared with an experimental result [54]. These two calculations give reasonable pressure on the front portion of the cylinder surface, however the magnitude of the minimum pressure and the base pressure on the cylinder are overpredicted. Moreover, Run **2** gives a closer result than Run **1** to the experimental result. The improvement in Run **2** demonstrates that improved results are achieved when the transition effect is accounted for.

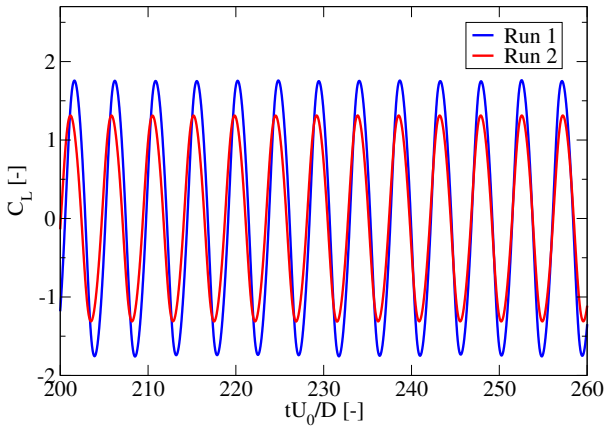

Figure 8: Comparison of lift coefficient with different wall boundary conditions for ω.

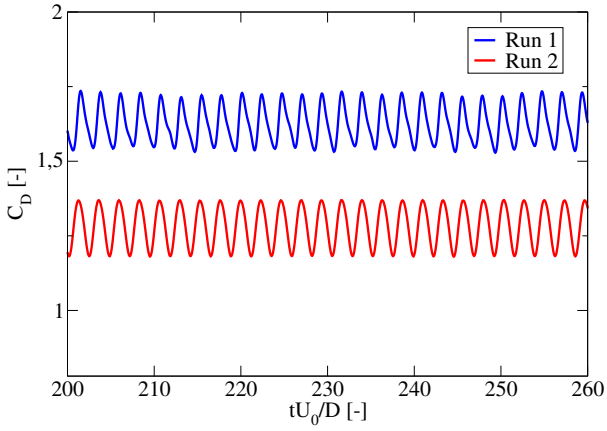

Figure 9: Comparison of drag coefficient with different wall boundary conditions for ω.

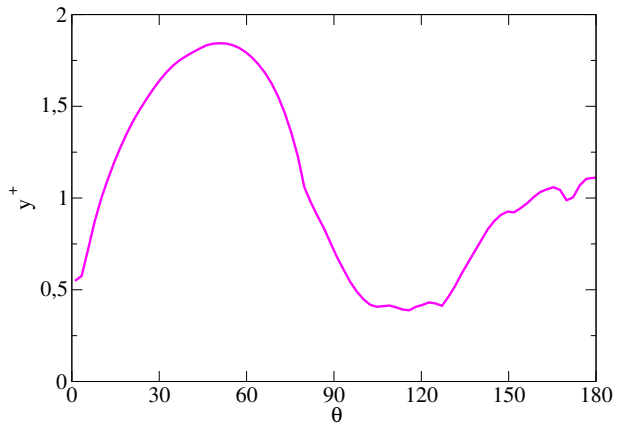

Figure 10: y^+ distribution around the cylinder for Run **1**.

Table 1: Reference data for flow past a fixed cylinder at $\mathrm{Re} = 10^4$: the Strouhal number St, drag coefficient C_D, r.m.s. lift coefficient $C_{L,\,\mathrm{rms}}$, and base pressure coefficient C_{p_b}.

References	L/D	St	C_D	$C_{L,\,\mathrm{rms}}$	$-C_{p_b}$
$k-\omega$ SST 2-D Unal et al. [30]	-	0.221	1.162	0.634	
DNS Dong et al. [25]	π	0.2	1.208	0.547	1.201
RANS Nguyen et al. [41]	6	0.2014	1.4101	0.9346	
DES Nguyen et al. [41]	6	0.1961	1.1329	0.3629	
Experiment Norberg [55]	$4-18$	0.2	-	0.394	
Experiment Bishop et al. [56]		0.2	1.1	0.6	

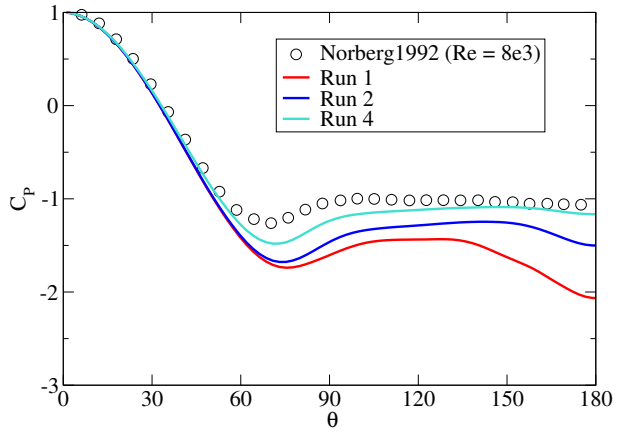

Figure 11: Comparison of mean pressure distribution on the cylinder.

4.1.2. 3-D simulation

A series of 3-D simulations (RANS) based on the $k-\omega$ SST model are performed. In Run **3**, only the basic turbulence model is used, while in Run **4** the transition correction model (25)-(27) is then tested, and in Runs **5** and **6** the curvature correction model (21) is applied with two different parameters for the turbulence production

Table 2: Numerical results from simulations of flow past a fixed cylinder at Re = 10^4: the Strouhal number St, drag coefficient C_D, r.m.s. lift coefficient $C_{L,\,\mathrm{rms}}$, and base pressure coefficient C_{p_b}.

Test case	Dimension	L/D	St	C_D	$C_{L,\,\mathrm{rms}}$	$-C_{p_b}$
DNS Dong et al. [25]	3-D	π	0.2	1.208	0.547	1.201
Run **1** (Menter's condition for ω_{wall})	2-D	-	0.217	1.627	1.253	1.435
Run **2** ($\omega_{\mathrm{wall}} = 10^{-12}$)	2-D	-	0.214	1.281	0.932	1.280
Run **3** (basic $k-\omega$ SST model)	3-D	π	0.210	1.175	0.759	
Run **4** (transition correction model)	3-D	π	0.207	1.154	0.683	1.105
Run **5** (curvature correction model 1)	3-D	π	0.213	1.155	0.712	
Run **6** (curvature correction model 2)	3-D	π	0.213	1.098	0.616	
Run **7** (LES)	3-D	π	0.212	1.105	0.364	
Run **8** (DES)	3-D	π	0.197	1.179	0.529	

limit $f_r^{\max}$. The resulting fluid forces from these runs are compared in Figures 12 and 13, and also in Table 2. As explained in [52], the addition of spanwise Reynolds stress components in 3-D simulation tends to cause a reduction in the lift and drag coefficients with respect to 2-D simulation, which can also be observed here in Run **3** compared to Run **2**. The transition correction model improves the numerical result in the sense that the results (see Table 2) are closer to the reference data listed in Table 1. The curvature correction model also influences the numerical results. Using $f_r^{\max} = 1.25$ as given by [35], the resulting force coefficients are decreased compared to Run **3**. Then using $f_r^{\max} = 1.4$, a result is obtained that lies in the reference data range shown in Table 1: $C_{L,\,\mathrm{rms}} \in [0.36 - 0.64]$ and $C_D \in [1.1 - 1.2]$.

The lift coefficient varies strongly for the simulations reported in Table 1. This could be due to the fact that different mesh resolutions are used in the spanwise direction. As shown in [25], the lift coefficient is highly sensitive to the mesh resolution whereas other physical quantities, e.g. the Strouhal number, drag coefficient are generally not influenced. For the cylinder with spanwise length $L = \pi D$ considered here, 32 space discretization steps are used. Moreover, it was observed in [41] that the aspect ratio L/D also has a large influence on the lift coefficient prediction. The comparison of pressure coefficient between the 2-D and 3-D simulations is shown in Figure 11. The 2-D simulation gives a larger magnitude for the base pressure coefficient, which corresponds to a larger drag coefficient, and the 3-D result is in better agreement with the experimental measured values.

A 3-D LES is also conducted using the Smagorinsky model (Run **7**). LES is well adapted for the present application where the flow is in the sub-critical regime [24, 28]. For LES, it is essential to consider a 3-D flow, as it is demonstrated in [24] that a 2-D LES yields unphysical results. Finally a DES model is used to simulate the flow in 3-D (Run **8**), where the near wall flow characteristics are modelled using the $k-\omega$ SST model, and the wake flow is resolved using a LES approach. Both LES and DES produce results in good agreement with the reference data, as can be seen in Table 2, where the numerical results are averaged over $200D/U_0$ time units. Figures 14 and 15 show respectively the comparison of lift and drag coefficients between RANS (Run **4**), LES and DES. The RANS predicts a well organised periodic flow, whereas the LES and DES results demonstrate irregular

turbulence characteristics. The small amplitude of the drag coefficient oscillation in RANS is coherent with its strongly dissipative nature [29]. Figure 16 presents a comparison of the mean streamwise velocity distribution for the RANS calculation and the LES. The two calculations produce nearly the same streamwise velocity distribution in upstream flow before the separation point, then after the separation, the LES gives a larger and much longer wake than the RANS calculation, which is different from a super-critical flow [29]. Contours of the instantaneous vorticity magnitude computed by RANS and LES at the middle spanwise plane are plotted in Figures 18 and 19. A vortex-shedding pattern can be observed in both results. The LES produces a less organized von Karman vortex street and a larger wake than the RANS calculation. Similar to the LES, the DES also produces a larger and longer wake than the RANS calculation, as shown in Figure 17. Figure 20 gives contours of the instantaneous vorticity magnitude computed using DES at the middle spanwise plane, which shows behaviour somewhere between LES and RANS in terms of wake size and regularity of the von Karman vortex street.

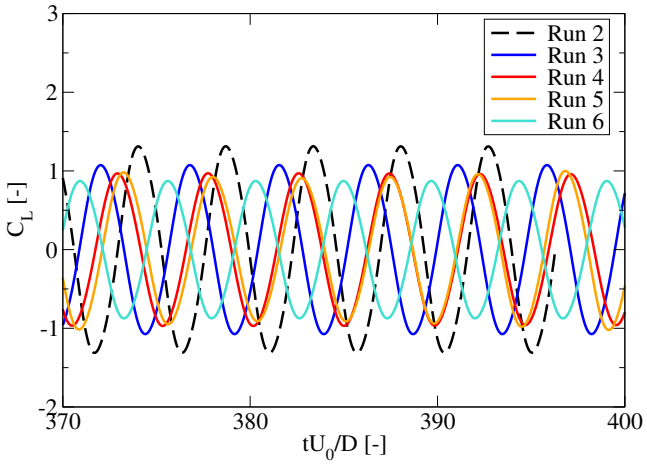

Figure 12: Time history of lift coefficients for different runs.

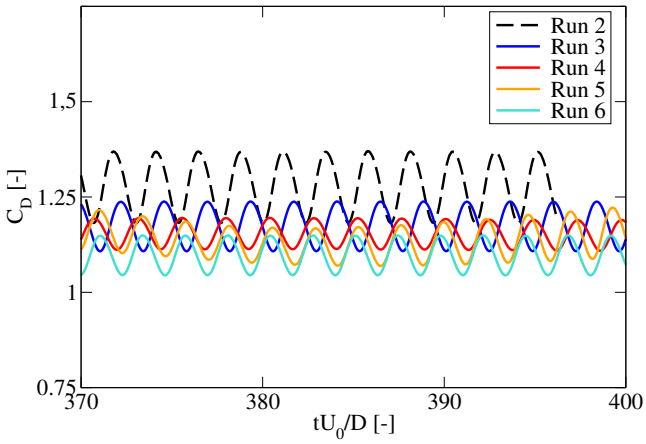

Figure 13: Time history of drag coefficients for different runs.

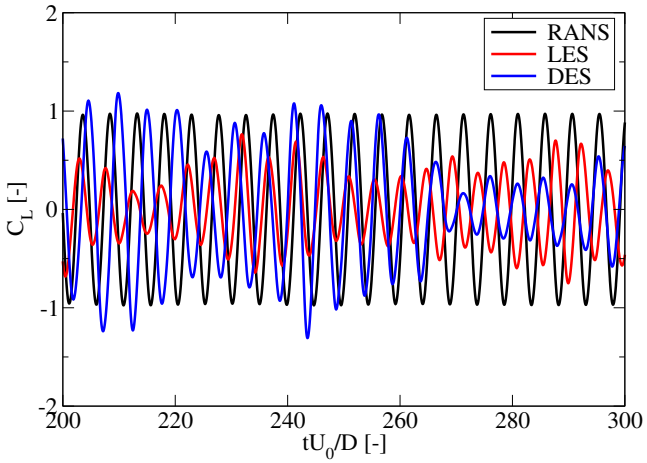

Figure 14: Comparison of time histories of lift coefficient.

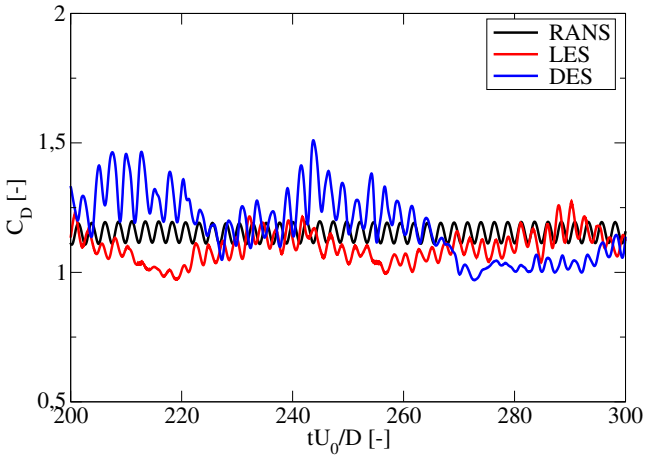

Figure 15: Comparison of time histories of drag coefficient.

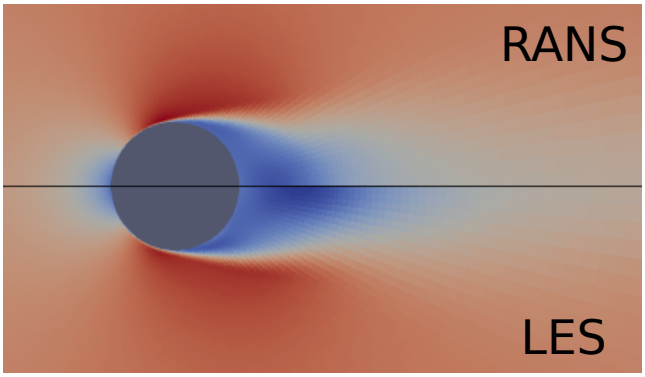

Figure 16: Comparison of mean streamwise velocity distribution, upper: RANS and lower: LES.

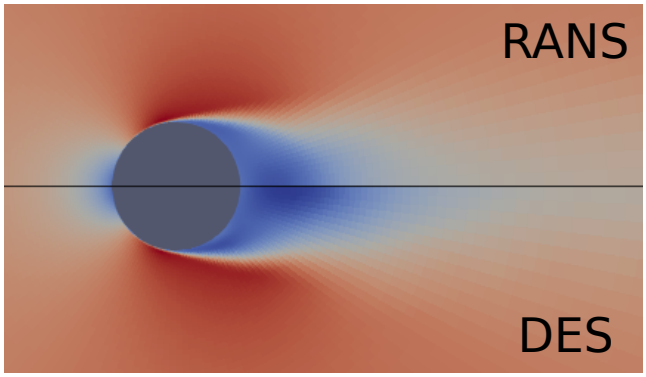

Figure 17: Comparison of mean streamwise velocity distribution, upper: RANS and lower: DES.

Figure 18: Instantaneous vorticity magnitude at the spanwise mid plane for a RANS simulation (Run **4**).

Figure 19: Instantaneous vorticity magnitude at the spanwise mid plane for a LES (Run **7**).

Figure 20: Instantaneous vorticity magnitude at the spanwise mid plane for a DES (Run **8**).

4.2. Flow over a flexibly mounted cylinder

This section presents the simulation of flow over a moving cylinder. This is an important element of the quasi-3D method which will allow calculation of the overall cable dynamics. Numerical results are shown to validate the moving reference frame approach and the turbulence models. VIV lock-in phenomenon, where the vibration frequency is independent of the external force and is instead equal to the natural frequency of the cylinder, is highlighted here.

4.2.1. Laminar case

First, we consider laminar cases where no turbulence model is needed. Two test cases are made:

a) Forced vertical oscillation. The rigid circular cylinder is subjected to a fixed vertical motion, and the fluid flow is in the horizontal direction. The vertical velocity of the cylinder is a function of time $u = 0.004\cos(12\pi t)$. In Figure 21, the lift and drag coefficients are compared with values found using the ALE method, which is available in Code_Saturne. These two numerical results agree well. Moreover, a spectral analysis of the resulting lift force gives a principal oscillation frequency of around 6 Hz, which corresponds to the frequency of the imposed cylinder motion. For the simulation of a physical time of 50 seconds, the CPU time used for the moving reference frame method and the ALE method is respectively about 29 minutes and 44 minutes, which indicates that the moving reference frame method is more efficient because it avoids the resolution of a moving mesh at each time step.

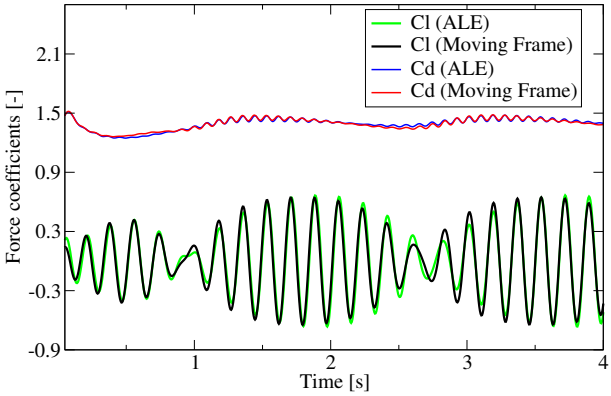

Figure 21: Comparison of lift and drag coefficients calculated using the moving reference frame method and the ALE method.

b) Free vertical oscillation. The moving reference frame approach is used to simulate a freely oscillating cylinder. The cylinder is initially fixed to allow the flow to become fully developed, then the cylinder is allowed to move in the transverse vertical direction using a mass-spring system. The set-up of the simulation is chosen to match the experimental work in [57] with mass ratio $m^* = \frac{m_L}{\rho D^2} = 234.2$, where m_L is the linear mass of the cylinder and the natural frequency of the cylinder is $f_n = 7.016$ Hz. These same parameters were also used in [58, 43, 59] for numerical investigation of VIV phenomenon. At Re = 90 the system is not in the lock-in regime and the transverse displacement is small, as shown in Figure 22 by the red line. At Re = 100, the system is in the lock-in regime, and the cylinder displacement reaches a peak amplitude of about 0.56 cylinder diameters, as shown in Figure 22 by the blue line. In addition frequency measurement of the displacement is equal to the natural frequency of the cylinder (mass-spring system), which confirms that this case lies within the lock-in regime. Whereas the vortex shedding frequency derived from the Strouhal number is $f = \frac{\mathrm{St}\, U_0}{D} = 6.548$ Hz. A series of calculations was performed with different Reynolds numbers in order to determine the lock-in range, and are compared with other works, as shown in Figure 23. The numerical results agree reasonably well with the experimentally measured values [57] and the numerical results in [59, 58], where large displacements that are taking place within the lock-in range are captured.

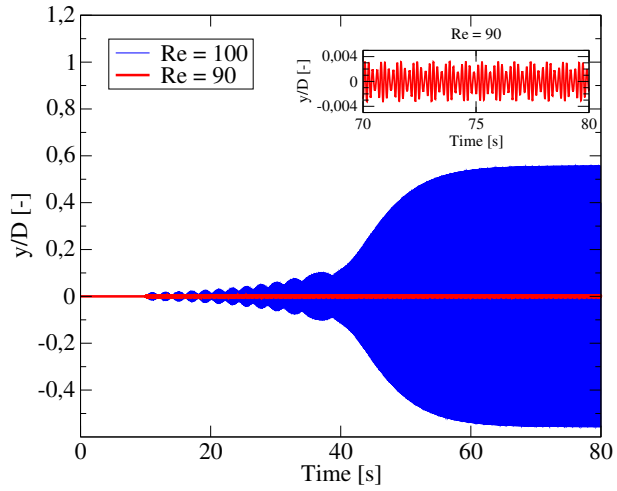

Figure 22: Temporal evolution of cylinder displacement at Re = 90 and Re = 100.

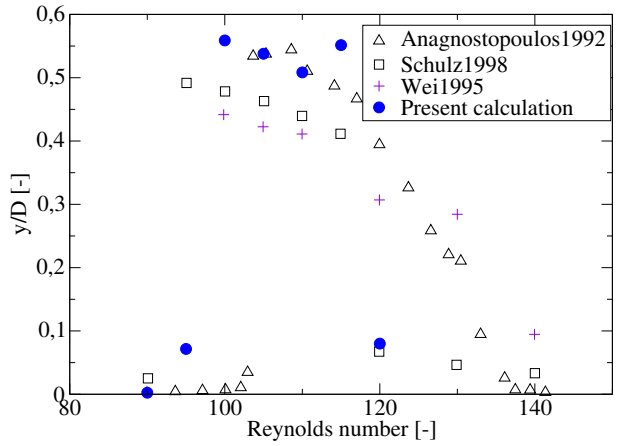

Figure 23: Lock-in range: comparison of cylinder displacements as function of the Reynolds number.

4.2.2. Turbulent case

Here we consider a turbulent flow over a rigid circular cylinder subjected to a fixed motion with the displacement as in [60, 25]

$$y = Y_0 D \cos(2\pi f_0 U_0 / D t), \tag{36}$$

where D is the cylinder diameter, $Y_0 = 0.3$ is the oscillation magnitude nondimensionalized using D, and f_0 is a nondimensional frequency.

Numerical results using LES and DES for a range of frequencies $f_0 \in \{0.14, 0.17, 0.19, 0.21, 0.25, 0.27, 0.30\}$ are compared with the experimental data in [60] and the DNS results in [25] in Figures 24 and 25. From the experimental data, one can observe an abrupt increase in the mean drag coefficient at $f_0 \approx 0.18$, whereas at other frequencies except high frequencies $f_0 > 0.3$ where there is a higher harmonic frequency, the mean drag coefficient is close to the stationary cylinder value. At low frequencies the lift coefficient magnitude increases slightly, and then rises sharply and reaches a peak at $f_0 \approx 0.18$ due to resonance between the vortex shedding and the imposed

motion. At higher frequencies the lift coefficient magnitude continues to rise steadily due to the effect of added mass [60].

In the LES the increase in the mean drag coefficient is captured but at a higher frequency $f_0 \approx 0.21$ than the reference data. The method detailed in [60, pp. 60-61] is used to determine the lift coefficient magnitude. The peak lift coefficient magnitude is attained at $f_0 \approx 0.19$, but with a magnitude much larger than the experimentally measured value. The fall in the lift coefficient after the peak and the increase at higher frequencies are well calculated by LES. For the DES, increase in the mean drag coefficient due to resonance is obtained at $f_0 \approx 0.19$, and the lift coefficient magnitude peak is observed at the same frequency. Globally, the numerical results agree reasonably well with the reference data.

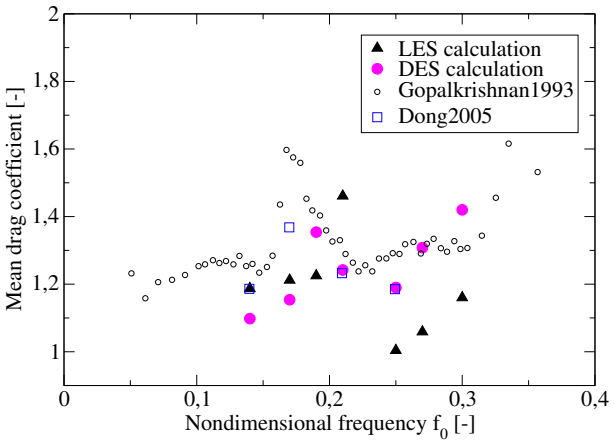

Figure 24: Mean drag coefficient as a function of nondimensional frequency f_0.

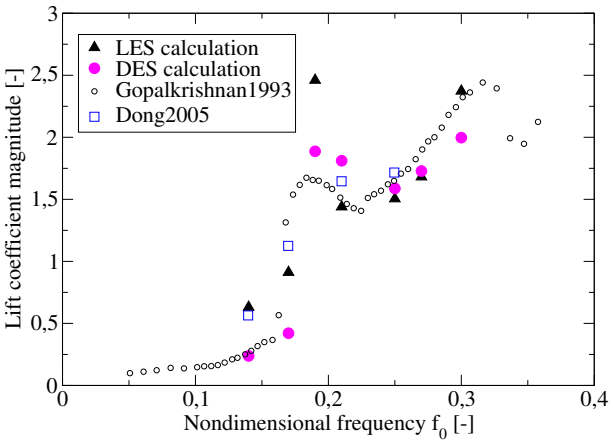

Figure 25: Lift coefficient magnitude as a function of nondimensional frequency f_0.

4.3. Cable dynamic

For the four test cases presented here, the cable is only allowed to move in the transverse direction of the fluid flow.

Case 1: 4 *nodes*

A very simple test case is performed in order to validate the MPI (Message Passing Interface) communication between the CFD instances. Four nodes are equally distributed along the cable, as shown in Figure 1 with $N = 4$. The two extremities are fixed by setting the corresponding displacements to $y_1 = y_4 = 0$. For interior nodes, from equation (3) with $L_s = \Delta z$ we have

$$M\frac{d^2y_2(t)}{dt^2} + Ky_2 = \frac{K}{2}y_3 + f_2, \tag{37}$$

$$M\frac{d^2y_3(t)}{dt^2} + Ky_3 = \frac{K}{2}y_2 + f_3, \tag{38}$$

where $M = m_L\Delta z$, $K = 2H/\Delta z$ and f_j is the fluid force applied to cylinder j.

By symmetry $y_2 = y_3$ and $f_2 = f_3$, so the movement of each cylinder satisfies

$$M\frac{d^2y_j(t)}{dt^2} + \frac{K}{2}y_j = f_j, \quad j \in \{2, 3\}. \tag{39}$$

One can remark that the movement of the two interior nodes is equivalent to that of a single flexibly mounted cylinder with mass M and stiffness $K/2$. The single flexibly mounted cylinder is simulated as a reference solution, which is compared with the coupled simulation using 4 nodes, as shown in Figure 26. Explicit and implicit coupled simulations are performed. In the explicit case, only one MPI communication is made between the cable solver and each fluid solver for each time step, thus the value at time instant t^n for y_j is used on right hand side of equations (37)-(38). For the implicit case, sub-iterations are used with multiple MPI communications to find a convergent solution of y_j at each time step. As shown in Figure 26, the numerical results using the coupled simulations are in good agreement with the reference solution, while they are further improved using the implicit method.

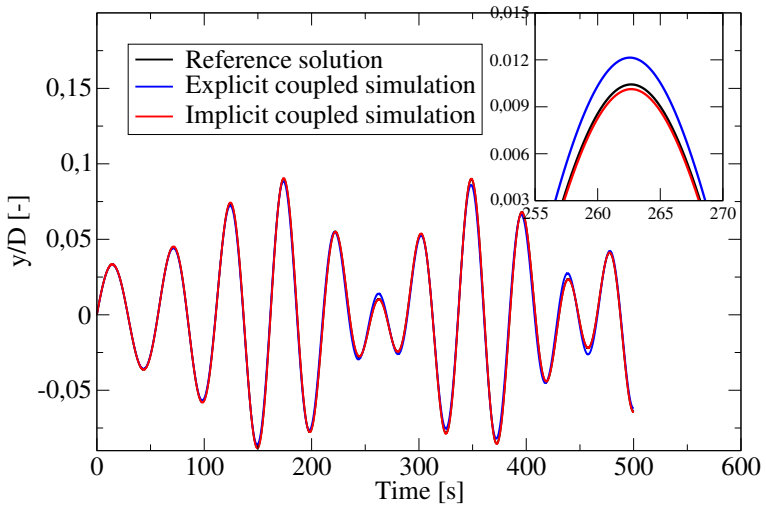

Figure 26: Comparison of displacements, where the reference solution is obtained using equation (39).

Case 2: $Re = 100$

As in [19, 44], the motion of a cable with spanwise length $L_z = 4\pi D$ and mass ratio $m^* = \frac{m_L}{\rho_f D^2} = 2$ is simulated using the quasi-3D method. Following [19] to determine the cable tension by considering a standing-wave response

$$y(z,\, t) = A\cos(\omega t)\cos(2\pi z/L_z), \tag{40}$$

to the cable equation (1). Substitution of the standing-wave response (40) into equation (1) by neglecting the bending stiffness C yields

$$\omega = \frac{2\pi}{L_z}\sqrt{\frac{H}{m_L}}. \tag{41}$$

For the first harmonic of VIV, it can be assumed that the frequency $f = \frac{\omega}{2\pi}$ of the standing-wave response is the same as that of the forcing due to vortex shedding on a circular cylinder with the same diameter, i.e. $f = \frac{\mathrm{St}\cdot U_0}{D}$. Hence the appropriate cable tension can be computed from $H = \left(\frac{\mathrm{St}\cdot U_0}{D} L_z\right)^2 m_L$. The flow for the present calculation is at Re = 100, the corresponding Strouhal number St = 0.167 for a fixed cylinder (an empirical relation between the Strouhal number and the Reynolds number can be found in [57]). Finally, using the quasi-3D method, the cable is decoupled into a series of cylinders, and each cylinder satisfies the mass-spring equation (3) with

$$M = m^* \rho_f D^2 L_s, \quad K = \frac{2HL_s}{(\Delta z)^2} = K^* \rho_f U_0^2 L_s, \tag{42}$$

where $K^* = 2\mathrm{St}^2 m^* \left(\frac{L_z}{\Delta z}\right)^2$, Δz is the distance between neighbouring cylinders (see Figure 1). Here we use 30 nodes and a periodic boundary condition to represent the cable. A non-dimensional time step of $\frac{U_0 \Delta t}{D} = 0.008$ is used giving about 750 time steps per shedding cycle. Figure 27 shows the temporal evolution of the displacement y/D along the cable, where a standing-wave response can be observed. This response is not stable and it transitions to a travelling wave later, as shown in Figure 28. The same cable behavior is obtained in the simulations of [19, 44]. In Figure 29 the power spectra density (PSD) of the displacement of an anti-node in the case of a standing wave and the PSD of the displacement of the same point in the case of a travelling wave are shown. The vibration frequencies are the same in the two cases, where $f_{\mathrm{cal}} \in [0.01953, 0.03906]\,\mathrm{Hz}$. The theoretical vortex shedding frequency based on the Strouhal number $f_{\mathrm{ref}} = 0.0267\,\mathrm{Hz}$, as represented by the dashed line, lies within the calculated frequency interval.

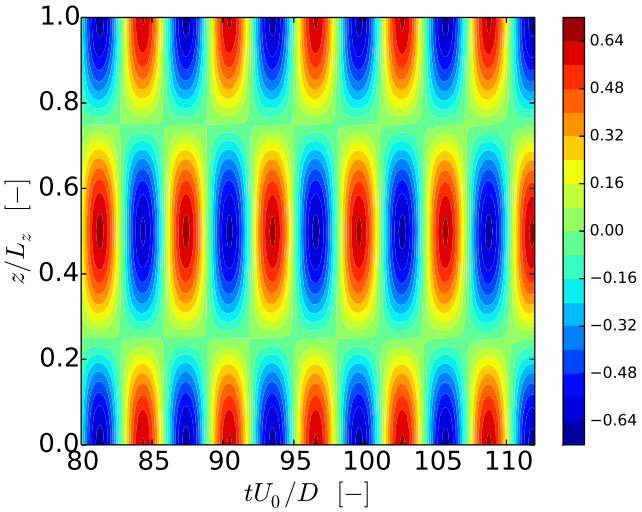

Figure 27: Early time history of displacement along the cable.

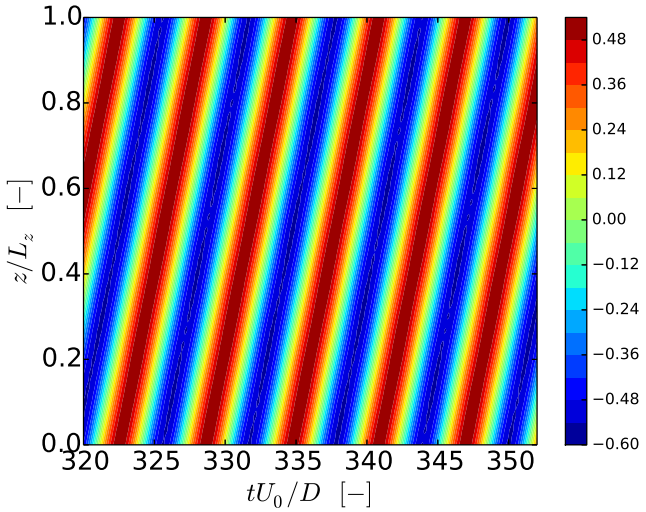

Figure 28: Later time history of displacement along the cable.

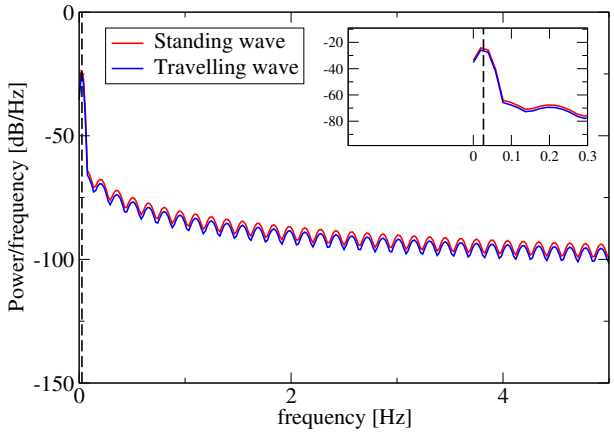

Figure 29: PSD of the displacement of an anti-node.

Case 3: linearly sheared inflow

A flexible riser subjected to currents with a linearly sheared velocity profile is simulated by [12]. The riser is allowed to vibrate in the transverse direction of the incoming flow with the two ends fixed. The inflow Reynolds number based on the cable diameter is Re = 200 at the top end of the riser and Re = 100 at the bottom end, giving Strouhal numbers in the range [0.167, 0.190] (the Strouhal number can be approximated as $\mathrm{St} = 0.212(1 - 21.2/\mathrm{Re})$ [57]). The aspect ratio of the riser is $L_z/D = 100$, the mass ratio $m^* = \frac{m_L}{\rho_f D^2} = 2.13$ and here 30 nodes are used to represent the long flexible cylinder. The fundamental modal frequency of the riser $f_1 = \frac{c}{2L_z}$, where $c = \sqrt{\frac{H}{m_L}}$ is the wave propagation speed in the riser, is chosen to be equal to the vortex shedding frequency at the mid-plane (Re = 150) in the spanwise direction of the riser $f_1 = \frac{\mathrm{St} \cdot U_{\mathrm{mid}}}{D}$.

Figure 30 shows a comparison of the rms displacement of the riser along the spanwise direction between the present work and the reference solution [12]. The two results have a similar fundamental mode form, and as in [12], the peak displacement is obtained towards the low Reynolds number end ($z = 44.8D$). The amplitude difference between the two results can be explained by the fact that different structural models are used, and in [12] the bending stiffness is also considered. Indeed, as shown in Figure 31, increased bending stiffness tends to reduce the displacement. And a rms displacement close to the reference solution is obtained with bending stiffness $C = 4C_0$, where $C_0 = 0.01HD^2$. Moreover, this test case is also simulated using the same wake oscillator model as in [9, 10], where a quasi-fundamental mode form is obtained with a peak displacement slightly towards the low Reynolds number end of the cable ($z = 47.9D$). Here in the wake oscillator calculation, the bending stiffness of the cable model is not considered. Figure 32 shows a comparison of the Strouhal number for flow around a stationary riser (dashed line, obtained using the above-mentioned empirical relation from [57]) and a vibrating riser (blue line). As expected, at the two ends the shedding frequencies are close in the two cases. Whereas far from the two ends, the shedding frequencies are significantly modified. The shedding frequencies away from the ends are locked to the fundamental frequency of the riser, as indicated by the superposition of the blue line and the red line in Figure 32, where the red line represents the Strouhal number calculated using the vibration frequency of the riser. Figures 33 and 35 show respectively the time evolution of the lift coefficient C_L and the displacement y/D. As in [12], we can observe an abrupt phase change in C_L at $z/L_z \approx 0.35$, where C_L and y/D are in phase at low Reynolds numbers, and are out of phase at high Reynolds numbers. The lift coefficient oscillations on the higher Reynolds number part of the riser are also much weaker, most likely due to the negative interaction between the cable motion and the vortex shedding. Figure 34 shows the time evolution of the lift coefficient along the cable calculated using the wake oscillator method, where no phase change in C_L is observed and the lift force frequency corresponds to that of the high Reynolds number end of the cable calculated using the quasi-3D method. The wake oscillator model yields a qualitatively correct vibration amplitude, however the phase change of the force along the cable is not well produced. Figure 36 shows the rms displacement of the riser along the spanwise direction with different numbers of sections N to represent the riser. As can be seen, use of $N = 30$ sections is enough to calculate accurately the cable dynamics, and increased N yields slightly greater displacements.

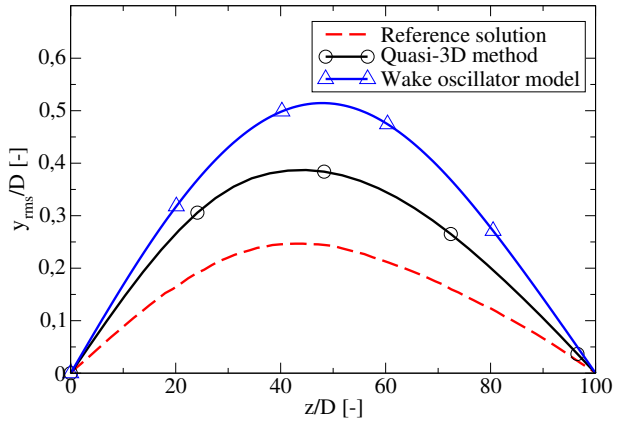

Figure 30: Rms displacement of the riser along the spanwise direction.

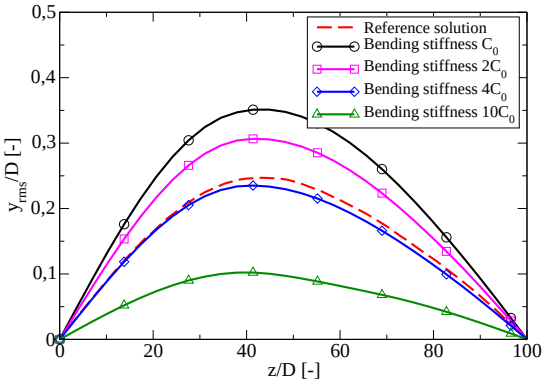

Figure 31: Rms displacement of the riser along the spanwise direction with different bending stiffness.

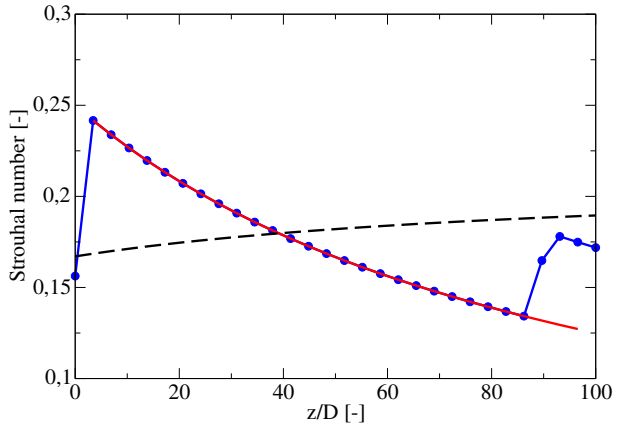

Figure 32: Comparison of the Strouhal number for flow around a stationary riser [57] (dashed line) and a vibrating riser (blue line). The red line is the Strouhal number at the riser frequency.

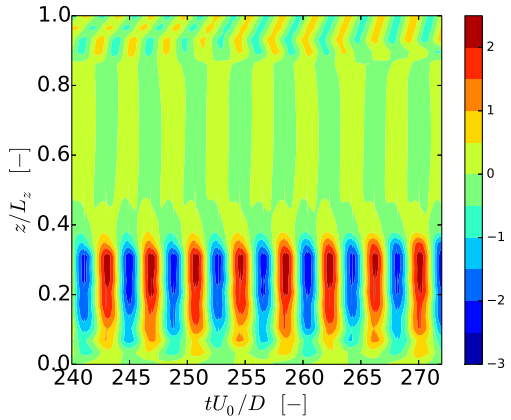

Figure 33: Time evolution of the lift coefficient along the riser calculated using the quasi-3D method.

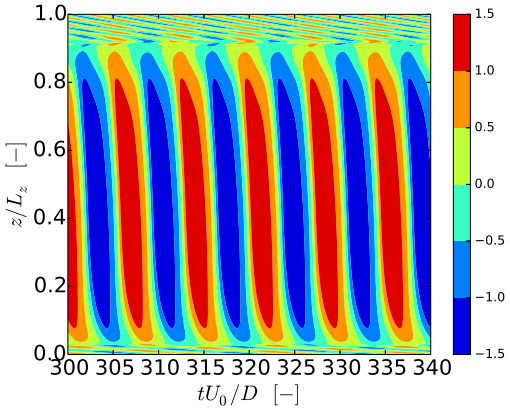

Figure 34: Time evolution of the lift coefficient along the riser calculated using the wake oscillator method.

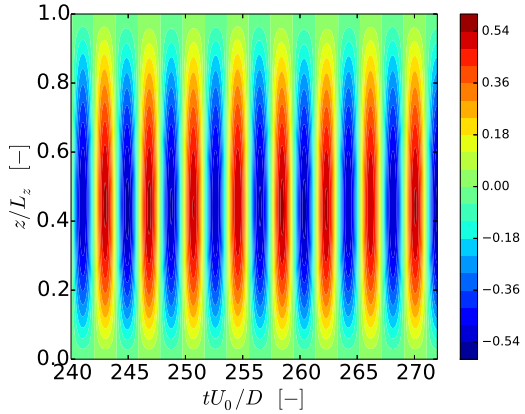

Figure 35: Time evolution of the riser displacement calculated using the quasi-3D method.

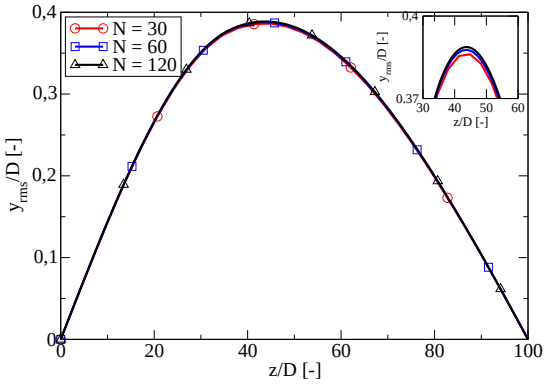

Figure 36: Rms displacement of the riser along the spanwise direction with different section numbers.

Case 4: linearly sheared turbulent inflow

This test case has been simulated using DNS in [61], where the cable is subjected to a linearly sheared flow, with the cable fixed at both ends. The inflow velocity satisfies $U_{\min} = 0.3U_{\max}$ and the maximal inflow velocity $U_{\max}$ corresponds to a cable diameter Reynolds number $\mathrm{Re} = 10^3$, hence in the turbulent regime. The cable characteristics are taken from [9]: the aspect ratio $L_z/D = 2028$, the mass ratio $m^* = m_L/(\rho D^2) = 2$, the dimensionless tension $\tilde{c} = \sqrt{\frac{H}{m_L}}\frac{1}{D\Omega_0} = 27.8$, where $\Omega_0 = \frac{2\pi \mathrm{St} U_{\max}}{D}$ is the angular frequency of the vortex shedding, and $\mathrm{St} = 0.2$ is the reference Strouhal number. Figure 37 shows the rms displacement of the cable along the spanwise direction. A standing wave response is observed at the two fixed ends and a travelling wave response is obtained away from the ends. The result obtained using the quasi-3D method agrees well with DNS at the high Reynolds number end of the cable. The difference between the two results at the low Reynolds number end of the cable could be due to the fact that in our quasi-3D calculation the $k-\omega$ SST turbulence model is used for the whole length of the cable, where the use of the turbulence model is not physically justified at low Reynolds numbers. No further investigation is conducted to get a closer numerical result compared to the DNS result because we are mainly interested in turbulent cases for future overhead conductor applications, and here we are only seeking a qualitative comparision with the DNS results. The same wake oscillator model for the fluid force as in [9, 10] is also used to simulate this test case, and the numerical result is qualitatively comparable to those of the quasi-3D method and the DNS. Moreover in the travelling wave region (away from the two ends) the quasi-3D method and the wake oscillator model give peak vibration amplitude towards the high Reynolds number end, whereas the DNS peak vibration amplitude is around the middle of the cable length. Figure 38 shows the PSD for the temporal evolution of the displacement of the cable section located at $z = 685D$, where a multi-modal response can be observed. The fundamental frequency of the riser is $f_1 = 0.199\,\mathrm{Hz}$, and the vortex shedding frequency based on the maximal inflow velocity is $f_{\mathrm{vortex}}^{\max} = 4.616\,\mathrm{Hz}$ using $\mathrm{St} = 0.2$, which corresponds to the 23rd mode. Figure 38 confirms that the number of modes excited is below 23. Figure 39 shows the rms displacements with different N to represent the cable, the displacements are globally close between the 3 cases, and increased N yields smoother rms displacements along the spanwise direction.

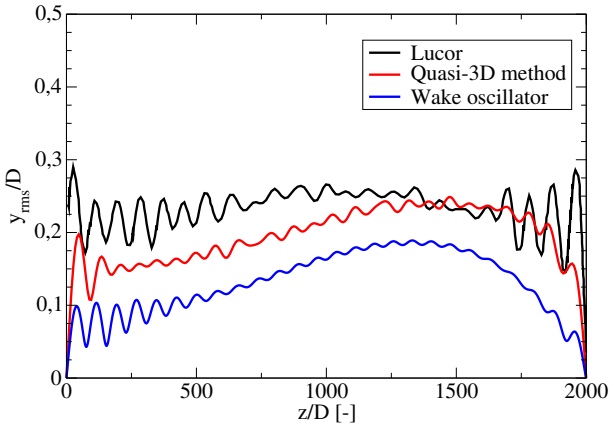

Figure 37: Rms displacement of the cable along the spanwise direction.

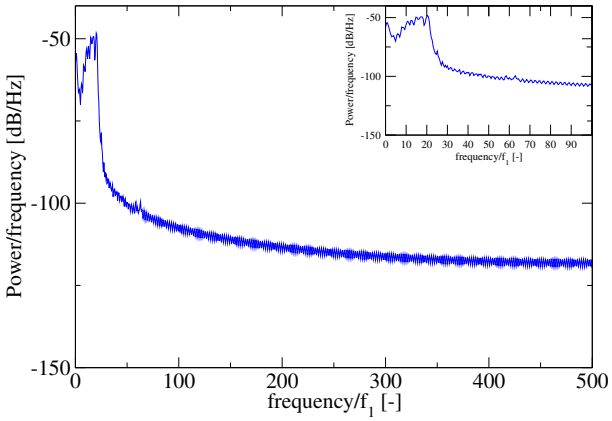

Figure 38: PSD of the temporal evolution of the displacement of the cable section located at $z = 685D$.

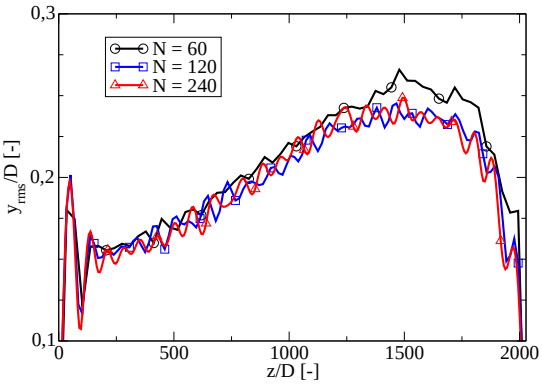

Figure 39: Rms displacement of the cable along the spanwise direction with different cable section numbers.

5. Conclusion

In this work, a quasi-3D method based on strip theory is used in order to simulate the effect of weak winds on overhead lines. This approach is necessary because fully 3-D simulation is not feasible. The quasi-3D method

transforms the overhead line model into a series of mass-spring systems with fluid effects appearing as an external force. The fluid flow simulation is carried out using the industrial Code_Saturne code and a moving reference frame approach is employed in order to avoid the use of a moving mesh for the fluid domain. The moving mesh method would be more costly and less robust. Turbulence models, including the $k-\omega$ SST model, the Smagorinsky model for LES and a DES model based on the $k-\omega$ SST model, are used to take into account the effect of turbulence in the flow.

Numerical simulations are conducted for flow around a stationary cylinder in order to validate the turbulence models. For 2-D simulation, the $k-\omega$ SST model with Menter's boundary condition for ω overpredicts the fluid force. Reynolds numbers are low in the current application, meaning that the flow is in the sub-critical regime. Hence, 3-D simulation is necessary to resolve influential spanwise flow structures along with transition correction models to better correspond with the sub-critical flow where transition occurs after separation. LES and DES give numerical results in good agreement with reference data. Flows over a flexibly mounted cylinder in both the laminar and turbulent regimes are then simulated in order to validate the moving reference frame method and the turbulence models in a moving frame. Finally, flexible cable dynamics were simulated using the quasi-3D method, yielding similar overall cable behavior to that found in the literature. These behaviors include a standing wave response that becomes unstable and transitions to a travelling wave in the case of an infinite cable, shedding frequencies that are locked to the natural frequency of the structure in the case of a riser subjected to a sheared flow, and a multi-modal VIV response that is observed in the case of a very high aspect ratio cable subjected to a turbulent sheared flow. In upcoming work, the numerical model presented in this paper will be further developed and integrated into a multi-scale numerical model for overhead conductors. The purpose of the multi-scale model is to assess the lifespan of overhead power lines due to mechanical fatigue phenomena [62, 63]. At the macro-scale level, for now, the EBP approach is used to calculate the dynamics of overhead conductors. Our aim is that the new model will be a more accurate and realistic alternative to the EBP approach.

Acknowledgements

This work was partially financed by RTE (Réseau de transport d'électricité) R&D.

Appendix A. Moving reference frame method

Appendix A.1. Moving reference frame for Navier-Stokes equations

A derivation of Navier-Stokes equations in a moving reference frame is given in this section based on the work of [43]. Here, only 2-D translations are considered, where the coordinates in the absolute reference frame are $(x_1^*,\, x_2^*)$ and the coordinates in the moving reference frame are $(x_1,\, x_2)$, so we have

$$\begin{cases} x_1^* = x_1 + d_1^s(t), \\ x_2^* = x_2 + d_2^s(t), \end{cases} \tag{A.1}$$

where $\mathbf{d}^s(t) = (d_1^s(t),\, d_2^s(t))^T$ is the displacement of the moving reference frame. It is first shown that the spacial gradient of a physical variable ϕ (e.g. P or u_j) is invariant with respect to the reference frame. For each variable

ϕ, the moving and fixed reference frames are related by the following equation:

$$\phi^*(x_1^*,\, x_2^*,\, t) = \phi(x_1,\, x_2,\, t) + \mathbf{a}_\phi \cdot \mathbf{u}^{\mathbf{s}}(t) = \phi(x_1^* - d_1^s(t),\, x_2^* - d_2^s(t),\, t) + \mathbf{a}_\phi \cdot \mathbf{u}^{\mathbf{s}}(t), \tag{A.2}$$

where $\mathbf{u}^s = \dot{\mathbf{d}}^s(t)$ is the velocity of the moving reference frame and the dot denotes a derivative with respect to time, $\mathbf{a}_\phi$ is a constant vector that has different values for each variable depending on whether the variable is affected by the moving reference frame. For example $\mathbf{a}_P = (0,\, 0)$ because the pressure is unaffected by the moving reference frame and $\mathbf{a}_{u_j} = \mathbf{e}_j$, where $\mathbf{e}_j$ is the unit vector in the direction x_j, because the velocity changes in the moving reference frame. Using the chain rule we have

$$\begin{aligned}\frac{\partial \phi^*(x_1^*,\, x_2^*,\, t)}{\partial x_j^*} &= \sum_{i=1}^{2} \frac{\partial \phi(x_1,\, x_2,\, t)}{\partial x_i} \frac{\partial x_i}{\partial x_j^*} + \frac{\partial \mathbf{a}_\phi \cdot \mathbf{u}^{\mathbf{s}}(t)}{\partial x_j^*} \\ &= \frac{\partial \phi(x_1,\, x_2,\, t)}{\partial x_j}.\end{aligned} \tag{A.3}$$

Similarly for the time derivative of the velocities, we have

$$\begin{aligned}\frac{\partial u_j^*(x_1^*,\, x_2^*,\, t)}{\partial t} &= \frac{\partial u_j(x_1,\, x_2,\, t)}{\partial t} + \sum_{i=1}^{2} \frac{\partial u_j(x_1,\, x_2,\, t)}{\partial x_i} \frac{\partial x_i}{\partial t}|_{x_1^*,\, x_2^*} + \dot{u}_j^s(t) \\ &= \frac{\partial u_j(x_1,\, x_2,\, t)}{\partial t} - \frac{\partial u_j(x_1,\, x_2,\, t)}{\partial x_i} u_i^s(t) + \dot{u}_j^s(t),\end{aligned} \tag{A.4}$$

The momentum equation in the absolute reference frame is

$$\frac{\partial u_j^*(x_1^*,\, x_2^*,\, t)}{\partial t} + u_i^* \frac{\partial u_j^*(x_1^*,\, x_2^*,\, t)}{\partial x_i^*} = -\frac{\partial P}{\partial x_j^*} + \nu \frac{\partial^2 u_j^*(x_1^*,\, x_2^*,\, t)}{\partial {x_i^*}^2}, \tag{A.5}$$

which in the moving reference frame becomes

$$\frac{\partial u_j(x_1,\, x_2,\, t)}{\partial t} + u_i \frac{\partial u_j(x_1,\, x_2,\, t)}{\partial x_i} = -\frac{\partial P}{\partial x_1} + \nu \frac{\partial^2 u_j(x_1,\, x_2,\, t)}{\partial x_i^2} - \dot{u}_j^s(t), \tag{A.6}$$

with the resulting new term $-\dot{u}_j^s(t)$.

Appendix A.2. Moving reference frame for turbulence models

The adjustments made to the turbulence models for the moving reference frame are now briefly explained. In RANS models the velocity is decomposed into a mean and a fluctuating part

$$\mathbf{u} = \mathbf{U} + \mathbf{u}', \tag{A.7}$$

where $\mathbf{U}$ can be obtained from an ensemble average for a given experiment over N realisations

$$\mathbf{U} = \lim_{N \to \infty} \frac{1}{N} \sum_{\alpha=1}^{N} \mathbf{u}^{(\alpha)}, \tag{A.8}$$

where α is the realisation index. A similar decomposition exists for the velocity $\mathbf{u}^*$ in the absolute reference frame. Differentiating equation (A.1) with respect to time gives the velocity relation in the two reference frames:

$$\mathbf{u}^* = \mathbf{u} + \mathbf{u}^s(t). \tag{A.9}$$

We follow [64] to show that the fluctuating velocity is frame invariant. The fluctuating velocity in the moving reference frame can be rewritten in three steps

$$\begin{aligned}\mathbf{u}' &= \mathbf{u} - \lim_{N\to\infty}\frac{1}{N}\sum_{\alpha=1}^{N}\mathbf{u}^{(\alpha)} \\ &= \mathbf{u}^* - \mathbf{u}^s(t) - \lim_{N\to\infty}\frac{1}{N}\sum_{\alpha=1}^{N}\left(\mathbf{u}^{*(\alpha)} - \mathbf{u}^s(t)^{(\alpha)}\right) \\ &= \mathbf{u}^* - \lim_{N\to\infty}\frac{1}{N}\sum_{\alpha=1}^{N}\mathbf{u}^{*(\alpha)}, \end{aligned} \tag{A.10}$$

where in the second step we have used the velocity relation (A.9), in the last step the velocity of the moving reference frame is cancelled because it is independent of the experimental realisations. The fluctuating velocity in the moving reference frame is therefore the same as in the absolute reference frame, hence the turbulent kinetic energy $k = \overline{u_i' u_i'}/2$. The turbulent dissipation rate $\varepsilon = \nu\overline{\frac{\partial u_i'}{\partial x_j}\frac{\partial u_j'}{\partial x_i}}$ is also frame invariant since it involves the fluctuating velocity and spatial derivatives. The frame invariance property is also valid for the specific turbulence dissipation rate $\omega = \varepsilon/k$. Using the chain rule for k and ω as has been done for the velocity in the previous section (see equations (A.3) and (A.4)), one can show that the transport equations for k and ω are frame indifferent [65]. For the Smagorinsky model the turbulent viscosity only depends on the strain rate tensor S_{ij}, therefore it is frame invariant [65].

Remark. In the absolute reference frame, the domain changes with time. Therefore in the Eulerian description of the domain $(x,\, t)$, we can have points which are in the fluid domain at some times and in the structure domain at other times, which makes ensemble averaging impossible in the derivation of turbulence models. In order to overcome this difficulty, one can consider deriving the physical equations in the time-independent ALE domain $(\chi,\, t)$ [42], with the help of a time-dependent mapping $x = A(\chi,\, t)$ to relate the Eulerian domain to the ALE domain. It should be noted that the ALE domain is different to the domain in the moving reference frame approach. In the former case the domain boundary remains the same with the time, whereas in the latter case the domain boundary changes with the time.

[1] J. Vecchiarelli, I. G. Currie, D. G. Havard, Computational analysis of aeolian conductor vibration with a stockbridge-type damper, Journal of Fluids and Structures 14 (2000) 489–509. doi:10.1006/jfls.1999.0279.

[2] CIGRE SC 22 WG 01: Report on aeolian vibration, ELECTRA, 41-77 (1989).

[3] B. Hübner, E. Walhorn, D. Dinkler, A monolithic approach to fluid-structure interaction using space-time finite elements, Computer Methods in Applied Mechanics and Engineering 193 (23-26) (2004) 2087–2104. doi:10.1016/j.cma.2004.01.024.

[4] U. Küttler, W. A. Wall, Fixed-point fluid-structure interaction solvers with dynamic relaxation, Computational Mechanics 43 (1) (2008) 61–72. doi:10.1007/s00466-008-0255-5.

[5] C. Habchi, S. Russeil, D. Bougeard, J.-L. Harion, T. Lemenand, A. Ghanem, D. Della Valle, H. Peerhossaini, Partitioned solver for strongly coupled fluid-structure interaction, Computers & Fluids 71 (2013) 306–319. doi:10.1016/j.compfluid.2012.11.004.

[6] C. Yvin, Couplage fluide-structure partitionné avec une chaîne de calculs open-source, in: 12è Journées de l'Hydrodynamique, 2010.

[7] Y. Jus, Modélisation et simulation numérique de vibrations induites par écoulements autour d'obstacles cylindriques seuls ou en réseaux, Ph.D. thesis, UPMC (2011).

[8] M. L. Facchinetti, E. de Langre, F. Biolley, Coupling of structure and wake oscillators in vortex-induced vibrations, Journal of Fluids and Structures 19 (2) (2004) 123–140. doi:10.1016/j.jfluidstructs.2003.12.004.

[9] R. Violette, E. de Langre, J. Szydlowski, Computation of vortex-induced vibrations of long structures using a wake oscillator model: Comparison with DNS and experiments, Computers and Structures 85 (11-14) (2007) 1134–1141. doi:10.1016/j.compstruc.2006.08.005.

[10] Y. Gao, Z. Zong, L. Zou, S. Takagi, Vortex-induced vibrations and waves of a long circular cylinder predicted using a wake oscillator model, Ocean Engineering 156 (2018) 294–305. doi:10.1016/j.oceaneng.2018.03.034.

[11] N. Srinil, M. Wiercigroch, P. O'Brien, Reduced-order modelling of vortex-induced vibration of catenary riser, Ocean Engineering 36 (17-18) (2009) 1404–1414. doi:10.1016/j.oceaneng.2009.08.010.

[12] R. H. J. Willden, J. M. R. Graham, Numerical prediction of VIV on long flexible circular cylinders, Journal of Fluids and Structures 15 (2001) 659–669. doi:10.1006/jfls.2000.0359.

[13] J. R. Meneghini, F. Saltara, R. de Andrade Fregonesi, C. T. Yamamoto, E. Casaprima, J. A. Ferrari, Numerical simulations of VIV on long flexible cylinders immersed in complex flow fields, European Journal of Mechanics B/Fluids 23 (2004) 51–63. doi:10.1016/j.euromechflu.2003.09.006.

[14] K. Herfjord, T. Holmas, K. Randa, A parallel approach for numerical solution of vortex induced vibrations of very long risers, in: Computational Mechanics - New Trends and Applications, 1998.

[15] Y. Duanmu, L. Zou, D.-c. Wan, Numerical simulations of vortex-induced vibrations of a flexible riser with different aspect ratios in uniform and shear currents, Journal of Hydrodynamics 29 (6) (2017) 1010–1022. doi:10.1016/S1001-6058(16)60815-6.

[16] R. H. J. Willden, J. M. R. Graham, Vortex induced vibration of deep water risers, in: The 7th International Conference on Flow-Induced Vibration, 2000, pp. 29–36.

[17] R. H. J. Willden, J. M. R. Graham, Multi-modal vortex-induced vibrations of a vertical riser pipe subject to a uniform current profile, European Journal of Mechanics - B/Fluids 23 (2004) 209–218. doi:10.1016/j.euromechflu.2003.09.011.

[18] R. H. J. Willden, J. M. R. Graham, CFD simulations of the vortex-induced vibrations of model riser pipes, in: 24th International Conference on Offshore Mechanics and Arctic Engineering, 2005.

[19] D. J. Newman, G. E. Karniadakis, A direct numerical simulation study of flow past a freely vibrating cable, Journal of Fluid Mechanics 344 (1997) 95–136. doi:10.1017/S002211209700582X.

[20] C. L. Lee, N. C. Perkins, Nonlinear oscillations of suspended cables containing a two-to-one internal resonance, Nonlinear Dynamics 3 (1992) 465–490.

[21] Eurobios Scientific Computing Branch, Mise en œuvre d'un modèle simplifié de vibration d'un conducteur et prise en compte des efforts issus du vent sur la portée, OLLA 2020 seminar No. 1, 2018.

[22] I. Celik, F. D. Shaffer, Long time-averaged solutions of turbulent flow past a circular cylinder, Journal of Wind Engineering and Industrial Aerodynamics 56 (2-3) (1995) 185–212. doi:10.1016/0167-6105(94)00091-Q.

[23] D. Lakehal, Computation of turbulent shear flows over rough-walled circular cylinders, Journal of Wind Engineering and Industrial Aerodynamics 80 (1-2) (1999) 47–68. doi:10.1016/S0167-6105(98)00122-6.

[24] M. Breuer, Large eddy simulation of the subcritical flow past a circular cylinder: numerical and modeling aspects, International Journal for Numerical Methods in Fluids 28 (9) (1998) 1281–1302.

[25] S. Dong, G. E. Karniadakis, DNS of flow past a stationary and oscillating cylinder at Re = 10000, Journal of Fluids and Structures 20 (2005) 519–531. doi:10.1016/j.jfluidstructs.2005.02.004.

[26] E. Achenbach, Influence of surface roughness on the cross-flow around a circular cylinder, Journal of Fluid Mechanics 46 (02) (1971) 321–335. doi:10.1017/S0022112071000569.

[27] C. Evangelinos, D. Lucor, G. E. Karniadakis, DNS-derived force distribution on flexible cylinders subject to vortex-induced vibration, Journal of Fluids and Structures 14 (2000) 429–440. doi:10.1006/jfls.1999.0278.

[28] M. Breuer, A challenging test case for large eddy simulation: high Reynolds number circular cylinder flow, International Journal of Heat and Fluid Flow 21 (2000) 648–654. doi:10.1016/S0142-727X(00)00056-4.

[29] P. Catalano, M. Wang, G. Iaccarino, P. Moin, Numerical simulation of the flow around a circular cylinder at high Reynolds numbers, International Journal of Heat and Fluid Flow 24 (2003) 463–469. doi:10.1016/S0142-727X(03)00061-4.

[30] U. O. Unal, O. Goren, Vortex shedding from a circular cylinder at high Reynolds number, in: Proc. 11th Int. Congress of the Int. Maritime Assn. of the Mediterranean, Lisbon, Maritime Transportation and Exploitation of Ocean and Coastal Resources, 2005, pp. 301–307.

[31] A. L. J. Pang, M. Skote, S. Y. Lim, Modelling high Re flow around a 2D cylindrical bluff body using the k-ω (SST) turbulence model, Progress in Computational Fluid Dynamics 16 (1) (2016) 48–57. doi:10.1504/PCFD.2016.074225.

[32] F. R. Menter, Two-equation eddy-viscosity turbulence models for engineering applications, AIAA Journal 32 (8) (1994) 1598–1605. doi:10.2514/3.12149.

[33] F. R. Menter, Zonal two equation $k-\omega$ turbulence models for aerodynamic flows, in: 23rd Fluid Dynamics, Plasmadynamics, and Lasers Conference, 1993. doi:10.2514/6.1993-2906.

[34] M. Kato, B. E. Launder, The modeling of turbulent flow around stationary and vibrating square cylinders, in: Ninth Symposium on Turbulent Shear Flows, 1993.

[35] P. E. Smirnov, F. R. Menter, Sensitization of the SST turbulence model to rotation and curvature by applying the Spalart-Shur correction term, in: ASME Turbo Expo, 2008.

[36] F. R. Menter, J. Carregal Ferreira, T. Esch, B. Konno, The SST turbulence model with improved wall treatment for heat transfer predictions in gas turbines, in: Proceeding of the International Gas Turbine Congress, 2003.

[37] F. Billard, J. M. Naughton, A. Revell, Unsteady RANS study of a flow past a vertical axis turbine, in: ERCOFTAC Symposium on Unsteady Separation in Fluid-Structure Interaction, 2013.

[38] S. Wang, D. B. Ingham, L. Ma, M. Pourkashanian, Z. Tao, Numerical investigations on dynamic stall of low Reynolds number flow around oscillating airfoils, Computers & Fluids 39 (9) (2010) 1529–1541. doi:10.1016/j.compfluid.2010.05.004.

[39] A. Travin, M. Shur, M. Strelets, P. Spalart, Detached-Eddy Simulations past a circular cylinder, Flow, Turbulence and Combustion 63 (1999) 293–313. doi:10.1023/A:1009901401183.

[40] F. R. Menter, M. Kuntz, R. Langtry, Ten years of industrial experience with the SST turbulence model, in: 4th International Symposium on Turbulence, Heat and Mass Transfer, 2003, pp. 625–632. doi:10.1.1.460.2814.

[41] V.-T. Nguyen, H. H. Nguyen, Detached eddy simulations of flow induced vibrations of circular cylinders at high Reynolds numbers, Journal of Fluids and Structures 63 (2016) 103–119. doi:10.1016/j.jfluidstructs.2016.02.004.

[42] J. Donea, A. Huerta, J.-P. Ponthot, A. Rodriguez-Ferran, Arbitrary Lagrangian-Eulerian methods, in: Encyclopedia of Computational Mechanics, John Wiley & Sons, 2004.

[43] L. Li, S. J. Sherwin, P. W. Bearman, A moving frame of reference algorithm for fluid/structure interaction of rotating and translating bodies, International Journal for Numerical Methods in Fluids 38 (2) (2002) 187–206. doi:10.1002/fld.216.

[44] Y. Bao, R. Palacios, M. Graham, S. Sherwin, Generalized thick strip modelling for vortex-induced vibration of long flexible cylinders, Journal of Computational Physics 321 (2016) 1079–1097. doi:10.1016/j.jcp.2016.05.062.

[45] R. A. Ibrahim, Nonlinear vibrations of suspended cables - Part III: Random excitation and interaction with fluid flow, Applied Mechanics Reviews 57 (2004) 515–549. doi:10.1115/1.1804541.

[46] R. W. Clough, J. Penzien, Dynamics of structures, 3rd Edition, Computers & Structures, Inc., 1995.

[47] F. Archambeau, N. Méchitoua, M. Sakiz, Code_Saturne: A finite volume code for the computation of turbulent incompressible flows - industrial applications, International Journal on Finite Volumes 1 (1) (2004) 1–62.

[48] R&D, EDF, Code_Saturne 5.0.9 Theory Guide (2018).

[49] K. Lodefier, B. Merci, C. De Langhe, E. Dick, Transition modelling with the SST turbulence model and an intermittency transport equation, in: ASME Turbo Expo, 2003.

[50] J. Smagorinsky, General circulation experiments with the primitive equations. Part I: The basic experiment, Monthly Weather Review 91 (3) (1963) 99–164. doi:10.1126/science.27.693.594.

[51] F. R. Menter, M. Kuntz, Adaptation of eddy-viscosity turbulence models to unsteady separated flow behind vehicles, in: The Aerodynamics of Heavy Vehicles: Trucks, Buses, and Trains, 2004, pp. 339–352.

[52] P. Batcho, G. E. Karniadakis, Chaotic transport in two- and three-dimensional flow past a cylinder, Physics of Fluids A 3 (5) (1991) 1051–1062. doi:10.1063/1.858085.

[53] M. Gramlich, Numerical investigations of the unsteady flow in the Stuttgart swirl generator with OpenFOAM, Master's thesis, Chalmers University of Technology (2012).

[54] C. Norberg, Pressure forces on a circular cylinder in cross flow, in: IUTAM Symposium Bluff-Body Wakes, Dynamics, and Instabilites, 1992, pp. 275–278. doi:10.1007/978-3-662-00414-2_60.

[55] C. Norberg, Fluctuating lift on a circular cylinder: review and new measurements, Journal of Fluids and Structures 17 (1) (2003) 57–96. doi:10.1016/S0889-9746(02)00099-3.

[56] R. E. D. Bishop, A. Y. Hassan, The lift and drag forces on a circular cylinder in a flowing fluid, Proceedings of the Royal Society A: Mathematical, Physical and Engineering Sciences 277 (1368) (1964) 32–50. doi:10.1098/rspa.1964.0004.

[57] P. Anagnostopoulos, P. W. Bearman, Response characteristics of a vortex-excited cylinder at low Reynolds numbers, Journal of Fluids and Structures 6 (1) (1992) 39–50. doi:10.1016/0889-9746(92)90054-7.

[58] R. Wei, A. Sekine, M. Shimura, Numerical analysis of 2D vortex-induced oscillations of a circular cylinder, International Journal for Numerical Methods in Fluids 21 (1995) 993–1005. doi:10.1002/fld.1650211016.

[59] K. W. Schulz, Y. Kallinderis, Unsteady flow structure interaction for incompressible flows using deformable hybrid grid, Journal of Computational Physics 143 (2) (1998) 569–597. doi:10.1006/jcph.1998.5969.

[60] R. Gopalkrishnan, Vortex-induced forces on oscillating bluff cylinders, Ph.D. thesis, Massachusetts Institute of Technology (1993).

[61] D. Lucor, H. Mukundan, M. S. Triantafyllou, Riser modal identification in CFD and full-scale experiments, Journal of Fluids and Structures 22 (6-7) (2006) 905–917. doi:10.1016/j.jfluidstructs.2006.04.006.

[62] J. Redford, M. Gueguin, M. Nguyen, H.-P. Lieurade, C. Yang, F. Hafid, J.-M. Ghidaglia, Calibration of a numerical prediction methodology for fretting-fatigue crack initiation in overhead power lines, International Journal of Fatigue 124 (2019) 400–410. doi:10.1016/j.ijfatigue.2019.03.009.

[63] J. Redford, H.-P. Lieurade, M. Gueguin, F. Hafid, C. Yang, J.-M. Ghidaglia, Modélisation numérique du phénomène de fretting-fatigue intervenant dans le vieillissement des conducteurs de lignes aériennes , Matériaux & Techniques 106 (3) (2018) 308. doi:10.1051/mattech/2018031.

[64] C. G. Speziale, Invariance of turbulent closure models, Physics of Fluids 22 (6) (1979) 1033–1037. doi:10.1063/1.862708.

[65] C. G. Speziale, Turbulence modeling in noninertial frames of reference, Theoretical and Computational Fluid Dynamics (1989) 3–19.